Binding affinities for 2D protein dimerization benefit from enthalpic stabilization

Adip Jhaveri[1], Smriti Chhibber[1], Nandan Kulkarni[1], Margaret E Johnson[1]*

[1]*TC Jenkins Department of Biophysics, Johns Hopkins University, 3400 N Charles St, Baltimore, MD 21218.*

**Corresponding Author*: margaret.johnson@jhu.edu

Abstract

The binding free energy between a protein dimer and its unbound monomers is primarily quantified in solution (3D), but several classes of soluble proteins, including those containing BAR domains, can also reversibly dimerize while bound to a membrane surface (2D). This 2D assembly process cannot be assigned the same free energy as in 3D due to restrictions to orientational motion and translation normal to the surface. The resulting ratio of dissociation constants, $\frac{K_D{}^{2D}}{K_D{}^{3D}}$, defines a lengthscale that is essential for determining whether dimerization is more favorable in solution or on the membrane surface. We show here using Molecular Dynamics simulations that changes to configurational sampling of even moderately flexible proteins can significantly alter the free energy landscape from 3D to 2D via not only the expected entropic restrictions, but due to enthalpic gains in the 2D bound ensemble. We simulated homodimerization between BAR-domain containing proteins in three distinct environments: in solution (3D), when bound to a lipid bilayer (2D), and when fully solvated but restrained to a pseudomembrane (2D). The free energy surfaces of both 2D systems are highly distinct from the 3D FES, selecting significantly better for the specific bound structure. We show that this is driven by stabilization of a new ensemble of monomer configurations that result in more enthalpically stable dimers states. Remarkably, performing this same procedure for a distinct parameterization of the BAR domain dimer shows much better agreement between the 3D and 2D FES, and this is supported by overall similarities in the enthalpies in both environments, highlighting the dependence of the FES on molecular structures. With $\frac{K_D{}^{2D}}{K_D{}^{3D}}$ ratios calculated here in the nanometer and lower regime for both dimers, at physiologic volume-to-surface-area ratios these proteins will both produce substantially more dimers on the membrane, which evolutionarily agrees with their function as membrane remodelers.

I. Introduction

The formation of reversible protein dimers from monomeric building blocks during membrane trafficking [1] [2, 3], signalling[4-6], and pattern formation[7, 8] is often of only moderate to weak stability, ranging from $K_D{}'s$ in the high nanomolar[9, 10] to high micromolar[11, 12], respectively. Forming a large population of dimers is then improbable without high concentrations that reach the micromolar range, were these proteins to operate in isolation. However, for many of the cytosolic proteins that participate in these membrane-dependent pathways, they also reversibly localize to membranes[13], often using domains such as the BAR domain studied here that directly bind membrane lipids[14]. These so-called peripheral membrane proteins will continue to diffuse on the membrane. Any two such localized monomers that could bind in 3D can now undergo reversible dimerization in the effectively 2D environment on the membrane. How will this surface localization alter dimerization strength and thus probability? The binding free energy of this reversible dimerization, ΔG^{2D} must change compared to ΔG^{3D} due to, at a minimum, entropy loss: the loss of a search dimension and the loss of unrestricted tumbling of monomers and dimers now adhered to a surface. A particularly useful metric for comparing these changes is the lengthscale $\frac{K_D{}^{2D}}{K_D{}^{3D}}$, as these dissociation constants are by definition independent of system size, whereas ΔG is not (the standard state in 3D is different than 2D). These metrics are related via $\frac{K_D{}^{2D}}{K_D{}^{3D}} = \frac{V}{SA}\exp\left(-(\Delta G^{2D}(SA) - \Delta G^{3D}(V))/k_{\mathrm{B}}T\right)$, where V and SA are the volume and surface area domains for measuring ΔG, k_{B} is Boltzmann's constant and T is temperature. How large do we expect this lengthscale range to vary due to additional entropic changes to backbone or sidechain sampling, protein-membrane interactions, or enthalpic changes? Here we generalize a statistical mechanical theory [15, 16] of the $\frac{K_D{}^{2D}}{K_D{}^{3D}}$ lengthscale to consider non-rigid proteins, with applications to peripheral membrane proteins. We specifically assess using MD simulations coupled to enhanced sampling[17] how these additional entropic or enthalpic factors control this lengthscale for the BAR-domain protein LSP1, which is known to dimerize in both 3D and 2D[18-20].

The magnitude of the $\frac{K_D{}^{2D}}{K_D{}^{3D}}$ lengthscale is especially critical for peripheral membrane proteins because they reside in the cytoplasm but can reversibly transition to membranes; this lengthscale is thus a key determinant in whether dimers will form more favorably in the cytoplasm (3D) or on the membrane (2D). For comparing a population of N dimer-forming proteins in a 3D volume V_1 vs a 2D area

SA_1, we are guaranteed to observe more dimers in 2D if the $\frac{K_D{}^{2D}}{K_D{}^{3D}} < \frac{V_1}{SA_1}$, which follows from the definition of the dissociation constant, $K_D{}^{3D} = \frac{N_{\text{mono}} N_{\text{mono}}}{V_1 N_{\text{dimer}}}$ or LeChatelier's principle[21]. More generally, for a population of proteins that can reversibly transition from V_1 to SA_1 (via lipid binding, for example), dimerization will be enhanced relative to 3D binding if $\frac{K_D{}^{2D}}{K_D{}^{3D}} < \frac{V_1}{SA_1}$, with the extent of enhancement depending in large part on the affinity of proteins for the membrane[22]. For peripheral membrane proteins that transition between the cytoplasm and the plasma membrane, $\frac{V_1}{SA_1} \sim \frac{R}{3}$, where R is the radius of the cell and thus on the order of μm. This means dimerization is enhanced on membrane surfaces when $\frac{K_D{}^{2D}}{K_D{}^{3D}}$ is below the μm scale, where we note that the smaller the lengthscale becomes, the more enhancement is observed on the membrane[22]. This dimensional reduction from a 3D to a 2D search for binding partners can thus dramatically enhance self-assembly, in addition to the well-established impact on search timescales[23, 24], but it depends on the thermodynamics of the specific binding pair.

The magnitude we expect for $\frac{K_D{}^{2D}}{K_D{}^{3D}}$ is roughly the nanometer scale, although several protein-specific and environmental factors will impact the order-of-magnitude. For adhesion proteins like Cadherin that bind across the gap between two cell membranes, this 'trans' contact was found through simulation and rigid-body approximations to be on the nanometer scale[25], but both the separation distance between the membranes and their roughness can lower the ratio by ~10 fold, with lower values reaching ~ 0.1nm for a rigid adhesion receptor of length 6nm[15, 16]. Binding across a membrane gap between non-adhesion protein pairs also found that the $K_D{}^{2D}$ relative to solution binding to the membrane-bound protein was ~1.5nm[26]. For peripheral membrane proteins, we did not find direct experimental quantification of $K_D{}^{2D}$; these proteins frequently transition between 2D and 3D which convolutes the binding measurements. However, several measurements of receptor interactions when bound to the same membrane are also nanometer scale [27-29]. For interferon receptor subunit binding to a ligand (that is restricted to 2D via another receptor subunit), $K_D{}^{2D}$ is ~1.2 x10^{-6} copies/nm^2, and with a $K_D{}^{3D} = 0.25uM$, the lengthscale $\frac{K_D{}^{2D}}{K_D{}^{3D}} = 8nm$. For the stronger subunit interaction, $K_D{}^{2D}$ is ~1.3 x10^{-7} copies/nm^2, but with a $K_D{}^{3D} = 7nM$ (4 x10^{-9} copies/nm^3) the lengthscale $\frac{K_D{}^{2D}}{K_D{}^{3D}} = 18nm$ [29]. Although the 2D and 3D K_D values are not entirely identical interactions due to the presence of a third protein in 2D that is not present in 3D, the dimer binding interface is likely conserved. 2D rates and dissociation

constants can also be extracted from model fits to in vitro measurements of assembly on membranes. From fluorescence data monitoring clathrin assembly on membranes in time[30], a best-fit value of the clathrin-clathrin interaction found $\frac{K_D{}^{2D}}{K_D{}^{3D}} \approx 30nm$. [31] This protein-protein interaction involves significantly larger proteins, as the clathrin trimer has a radius of ~$17nm$ [32] and the proteins are flexibly tethered to the membrane surface via recruitment from (at least one) other protein[1]. Collectively, these studies support ratios of $\frac{K_D{}^{2D}}{K_D{}^{3D}}$ in the $0.1 - 50nm$ range for functionally relevant 2D interactions. However, physically both larger and smaller ratios are possible. If membrane binding occludes the protein-protein interface, we expect the ratio to rise to effectively $\frac{K_D{}^{2D}}{K_D{}^{3D}} \to \infty$, since no specific binding will occur in 2D. Partial occlusion of the binding site would thus trend towards the μm regime. Alternatively, if membrane binding induces conformational changes in the proteins[33] that improve the binding interface, this could similarly change the enthalpy of the binding interaction and drive $\frac{K_D{}^{2D}}{K_D{}^{3D}}$ to the subnanometer regime. Here we find that for the LSP1 dimer in the coarse-grained MARTINI 3 forcefield[34], the lengthscale is quite low (subnanometer), driven by changes to the monomer configurations sampled in 2D that support enthalpic gains in stabilization when the monomers bind. Remarkably, this same dimer simulated in the MARTINI 2 forcefield instead produces a signficantly higher ratio, back to the nanometer range. While this clearly indicates force-field dependencies[35], the rich data from the simulations allows us to attribute this variation to differential contributions of enthalpic vs entropic terms.

The advantage of simulation and theory for characterizing this key metric is threefold—with simulation (i) we can study exactly two proteins and thus avoid oligomer formation, (ii) we can readily discard parts of the trajectory where the proteins depart from the 2D membrane and (iii) we obtain high-resolution structural and energetic details on both the bound and unbound ensembles. This provides us the first quantitative estimates of $K_D{}^{2D}$ for this essential family of protein domains, and simultaneously provides mechanistic insight into the magnitude of $\frac{K_D{}^{2D}}{K_D{}^{3D}}$ resulting from entropic and enthalpic terms. By using the relatively high-resolution MARTINI coarse-grained force-field, our simulations retain explicit solvent and flexibility of the protein backbone and side chains. Because previous simulation studies of 2D dimerization (in trans) used rigid protein domains with limited interdomain flexibility and no solvent[15, 16, 25], this allows us to consider entropy changes arising from far more degrees of freedom. Importantly, we also relax the assumption that the enthalpy of the

interaction is unchanged, such that if new conformations are sampled in 2D with lower potential energy, that will further stabilize the 2D bound state. From Molecular Dynamics simulations, we construct a free energy surface (FES) via the metadynamics enhanced sampling method, which is readily accessible from the PLUMED software[36] with GROMACs simulations[37]. In recent work we used this same approach to characterize the FES and ${K_D}^{3D}$ of the LSP1 dimer in solution using the MARTINI 2 force-field, finding that the monomers engage in several nonspecific bound dimer states in addition to the known crystal structure[38]. We predicted that several of these bound states would be lost in a 2D ensemble, which we find here is indeed the case, as these diverse structures engaged the membrane-binding residues in protein-protein interfaces. We take advantage of restraints available in MD simulations to construct a 'pseudomembrane' simulation, retaining 2D restrictions to translational and orientational motion, but without the explicit membrane environment. We thus control for whether the membrane surface charge or curvature changes substantially impact the 2D FES.

II. THEORY

II.A Theoretical background on binding thermodynamics

The equilibrium constant for a pair of protein monomers binding to one another in solution (3D) is given by:

$$ {K_D}^{3D} = V^{-1} \exp\left(\frac{\Delta G(V)}{k_{\mathrm{B}} T}\right) \#(1) $$

Where k_{B} is Boltzmann's constant, V is the system volume, T is the temperature, and ΔG is the Gibb's free energy difference between two states, the bound and unbound monomers, $\Delta G(V) = G_{bnd}(V) - G_{unb}(V)$ at a constant NPT, N particle number and P pressure. The Gibb's free energy for a state s depends on the Helmholtz free energy A_s via $G_s = A_s + PV_s$, thus the free energy difference is:

$$ \Delta G(V) = \Delta A(V) + P\Delta V \#(2) $$

where ΔA and ΔV report the difference between the bound and unbound states.

The standard state free energy G_s^0 of either state ($N_s = 1$ for s = bound dimer, and $N_s = 2$ for s = unbound monomers) can always be computed using $G_s(V_s) = G_s^0(V^0) + N_s k_\mathrm{B} T \ln\left(\frac{V^0}{V_s}\right)$. The binding free energy thus scales with volume as $\Delta G(V_1) = \Delta G(V_2) + k_\mathrm{B} T \ln\left(\frac{V_{2,bnd} V_{1,unb}^2}{V_{1,bnd} V_{2,unb}^2}\right)$, and simplifies when the volume is the same in the bound and unbound ensemble, $V_{bnd} \cong V_{unb}$, to:

$$\Delta G(V_1) \cong \Delta G(V_2) - k_\mathrm{B} T \ln\left(\frac{V_2}{V_1}\right) \#(4)$$

We include this well-known result to emphasize how the binding free energy of the system will become more positive linearly with respect to the logarithm of the increased volume in 3D. This is because larger volume stabilizes the unbound state more than the bound state. We report the ΔG values for our given system V, which defines the same K_D as the standard state via Eq. 1.

From Eq. 2, the primary determinant of the binding free energy ΔG is through A, which is calculated from the canonical partition function Q via:

$$A = -k_B T \ln(Q) \#(4)$$

The contribution of $P\Delta V$ in Eq. 2 is typically negligible compared to the change in internal energy and entropy of the bound and unbound states, so we assume it can be neglected, $V_{bnd} \cong V_{unb}$, and $\Delta G(V) \cong \Delta A(V)$. The (dimensionless) partition function is defined for a system of N particles using,

$$Q = \frac{1}{n_S! h^{3N}} Z_p(\{\boldsymbol{p}^N\}) Z(\{\boldsymbol{r}^N\}) \#(5)$$

where h is Planck's constant and there will be an indistinguishability factor for (at least) the n_S solvent particles. $Z_p(\{\boldsymbol{p}^N\})$ is the momentum integral, which we assert will remain the same value for bound and unbound ensembles, given the fixed temperature. $Z(\{\boldsymbol{r}^N\})$ is the configuration integral dependent on positions $\boldsymbol{r}$ of all N particles, which differs between bound and unbound ensembles, and differs as membrane localization restricts protein positions in the volume. The ratio of the bound and unbound partition functions Q_{bnd}/Q_{unb} will thus reduce to the ratio of the bound and unbound configuration integrals:

$$\Delta A(V) = -k_B T \ln\left(\frac{Z_{bnd}(\{\boldsymbol{r}^N\})}{Z_{unb}(\{\boldsymbol{r}^N\})}\right) \#(6)$$

Both Z_{bnd} and Z_{unb} depend on the system volume, but most of those factors cancel out when taking their ratio. In 3D, the configurational sampling of two monomers in the unbound state (versus one dimer in the bound state) preserves the dependence of ΔA on V. Eq 6 differs from a similar result, Eq 13 in Ref[39], because there the contributions to the binding free energy were derived based on an unbound state with each protein in an isolated volume.

II.B Theoretical background on the 2D binding equilibrium constant

The binding free energy between a pair of protein monomers that are restricted to a membrane/surface no longer scales with the volume of the system as defined in Eq. 4. As the height of the system increases, the ΔG should not change, as the additional solvent volume is not sampled by either the bound or unbound monomers and thus does not contribute to the relative free energy. Increases to the surface area, SA, however, will change ΔG due to increased space for both unbound monomers. Thus, we must assert the system as being restricted to effectively 2D sampling; the proteins cannot unbind from the membrane. The 2D dissociation constant is then given by:

$$K_D{}^{2D} = SA^{-1} \exp\left(\frac{\Delta G(SA)}{k_B T}\right) \#(7)$$

Compared to Eq. 4, the relative free energy for surface-restricted binding would instead scale as $\Delta G(SA_1) \cong \Delta G(SA_2) - k_\mathrm{B} T \ln\left(\frac{SA_2}{SA_1}\right)$, where we assumed $SA_{bnd} = SA_{unb}$ for both volumes. The molecules still exist in 3D space, of course, and so the partition functions of Eq. 6 are still defined over the same protein degrees of freedom as in 3D, but with restrictions to the height of the proteins within the volume to enforce a 2D search. These restrictions to the surface then further limit rigid-body orientational sampling, as proteins align a specific interface to the

membrane, and they may also restrict configurational sampling of the protein's internal degrees of freedom.

The ratio of 3D and 2D equilibrium constants for a pair of protein monomers gives:

$$\frac{{K_D}^{2D}}{{K_D}^{3D}} = \frac{V}{SA}\exp\left(\frac{-\left(\Delta G^{3D}(V) - \Delta G^{2D}(SA)\right)}{k_B T}\right) \#(8)$$

Inserting Eq. 2 and Eq. 6 into this formula, and ignoring/cancelling the $P\Delta V$ terms for 2D and 3D produces:

$$\frac{{K_D}^{2D}}{{K_D}^{3D}} = \frac{V}{SA}\frac{{Z_{bnd}}^{3D}(V)}{{Z_{unbnd}}^{3D}(V)}\frac{{Z_{unbnd}}^{2D}(SA)}{{Z_{bnd}}^{2D}(SA)} \#(9)$$

Where here the ratio of the 2D partition functions, $\frac{{Z_{unb}}^{2D}}{{Z_{bnd}}^{2D}}$, is written based on its dependence on the system SA, due to the cancellation of terms depending on the system height, as we show below.

II.C Theoretical background on the 3D and 2D partition functions

To simplify the definition of the 2D vs 3D binding constant in Eq. 9, we first make essentially exact simplifications to the partition functions. Using similar notation to Ref[39] and [40], we note that performing the integral over all particle positions in the volume is much more insightful when adopting a coordinate system that defines the $N1$ internal coordinates of protein 1, $(\boldsymbol{r_1}^{\boldsymbol{N1}})$**,** of protein 2, $(\boldsymbol{r_2}^{\boldsymbol{N2}})$ **,** of the solvent particles $(\boldsymbol{r_s}^{\boldsymbol{Ns}})$, and of membrane coordinates $(\boldsymbol{r_m}^{\boldsymbol{Nm}})$, relative to the translational positions and orientations of proteins 1 and 2 in the system volume. We will simplify the notation of internal coordinates further to $\boldsymbol{r_1}, \boldsymbol{r_2}, \boldsymbol{r_{s,m}}$ for compactness, with no membrane coordinates in the 3D system. The translational position and rigid-body orientation of protein 1 in the volume are given by $\boldsymbol{R}_1$, $\boldsymbol{\Omega}_1$ respectively. The relative position of

protein 2 to 1 are then given by $\boldsymbol{R}_{21} = [x_{21}, y_{21}, z_{21}]$, with protein 2's rigid-body orientation as $\boldsymbol{\Omega}_2$. The configuration integrals are then defined as

$$Z_{unb} = \int_V d\,\boldsymbol{R}_1 \int d\,\boldsymbol{\Omega}_1 \int_V d\,\boldsymbol{R}_{21} \int d\,\boldsymbol{\Omega}_2 \int d\boldsymbol{r_1} d\boldsymbol{r_2}\, d\boldsymbol{r_{s,m}} H(|\boldsymbol{R}_{21}| - r_{cut}) \exp\left(-\beta U\left(\boldsymbol{R}_1, \boldsymbol{\Omega}_1, \boldsymbol{r_1}, \boldsymbol{r_2}, \boldsymbol{r_{s,m}}, \boldsymbol{R}_{21}, \boldsymbol{\Omega}_2\right)\right) \quad (10a)$$

$$Z_{bnd} = \int_V d\,\boldsymbol{R}_1 \int d\,\boldsymbol{\Omega}_1 \int_V d\,\boldsymbol{R}_{21} \int d\,\boldsymbol{\Omega}_2 \int d\boldsymbol{r_1} d\boldsymbol{r_2}\, d\boldsymbol{r_{s,m}} H(r_{cut} - |\boldsymbol{R}_{21}|) \exp\left(-\beta U\left(\boldsymbol{R}_1, \boldsymbol{\Omega}_1, \boldsymbol{r_1}, \boldsymbol{r_2}, \boldsymbol{r_{s,m}}, \boldsymbol{R}_{21}, \boldsymbol{\Omega}_2\right)\right) \quad (10b)$$

where *H* is the Heaviside function used to designate each configuration to either the bound or unbound ensemble, and $\beta = 1/k_B T$. We use r_{cut} as a distance separation to distinguish the bound dimer from two non-interacting monomers, which may generally be dependent on the internal coordinates of both monomers, their hydration solvent, and their relative orientations, $r_{cut} = r_{cut}\left(x_{21}, y_{21}, z_{21}, \boldsymbol{\Omega}_2, \boldsymbol{r_1}, \boldsymbol{r_2}, \boldsymbol{r_{s,m}}\right)$, with this volume then defined as V_{cut}. While we treat the two monomers as distinct in this derivation for labeling clarity, the results are the same for homo-dimers. This is a two-state separation of state-space via configurations, so collectively they sum: $Z = Z_{bnd} + Z_{unb}$.

We first expand the integrals over $\boldsymbol{R}_1$, the position of 1 in the volume, using Cartesian coordinates as x_1, y_1, z_1 that each span a boxlength L in 3D, and $\boldsymbol{\Omega}_1$ the rigid-body orientation of molecule 1 at a given position, using the Euler/Tait-Bryan convention with Ψ_1 the yaw, Θ_1 the pitch, and Φ_1 the roll. These angles describe intrinsic rotations around the molecule's internal coordinate system z, y', x'', just as for an airplane (where y' is the axis after the first rotation, x'' is after two rotations), as illustrated in Figure 1. We rewrite Eq. 10 for each of the two states s as:

$$Z_s = \int_0^L \mathrm{d}z_1 \int_0^L dy_1 \int_0^L dx_1 \int_0^{2\pi} d\Psi_1 \int_0^{2\pi} d\Phi_1 \int_0^{\pi} \sin(\Theta_1)\, d\Theta_1 Z_{21,s} \;\#(11a)$$

$$Z_{21,bnd} = \int_V d\,\boldsymbol{R}_{21} \int d\,\boldsymbol{\Omega}_2 \int d\boldsymbol{r_1} d\boldsymbol{r_2}\, d\boldsymbol{r_{s,m}} H(r_{cut} - |\,\boldsymbol{R}_{21}|) \exp\left(-\beta U\left(\boldsymbol{R}_1,\, \boldsymbol{\Omega}_1, \boldsymbol{r_1}, \boldsymbol{r_2}, \boldsymbol{r_{s,m}}, \boldsymbol{R}_{21},\, \boldsymbol{\Omega}_2\right)\right) \#(11b)$$

Where $Z_{21,s}$ contains all the remaining integrals from Eq. 10 that define the relative configurations between the two monomers and their internal coordinates. For a protein 1 that is free to diffuse in all 3 dimensions, the system's potential energy does not depend on its translational position or rigid body orientation within the volume (e.g. there are no boundary effects). Thus we can simplify the potential energy function of Eq 11b to $U\left(\boldsymbol{r_1}, \boldsymbol{r_2}, \boldsymbol{r_{s,m}}, \boldsymbol{R}_{21}, \boldsymbol{\Omega}_2\right)$ and immediately perform the integrals in Eq. 11a to get for 3D:

$$Z_s^{3D} = 8\pi^2 V\, Z_{21,s}^{3D} \#(12)$$

For the ratio of the 3D partition functions in Eq.9, this $8\pi^2 V$ factor drops out. Following this integration over protein 1's position and orientation, we can now consider its central position and orientation fixed in the box, and the integrals over $\boldsymbol{R}_{21}$ and $\boldsymbol{\Omega}_2$ thus occur over x_{21}, y_{21}, z_{21}, and Ψ_2 the yaw, Θ_2 the pitch, and Φ_2 the roll of protein 2. For the bound state partition function, 11b is then written as,

$$Z_{21,bnd}^{3D} = \int_0^L dz_{21} \int_0^L dy_{21} \int_0^L dx_{21} \int_0^{2\pi} d\Psi_2 \int_0^{2\pi} d\Phi_2 \int_0^{\pi} \sin(\Theta_2)\, d\Theta_2 \int d\boldsymbol{r_1} d\boldsymbol{r_2}\, d\boldsymbol{r_{s,m}} H(r_{cut} - |\,\boldsymbol{R}_{21}|) \#$$

$$\exp\left(-\beta U\left(\boldsymbol{r_1}, \boldsymbol{r_2}, \boldsymbol{r_{s,m}}, \boldsymbol{R}_{21}, \boldsymbol{\Omega}_2\right)\right) \quad (13)$$

No further simplifications are possible here for the bound state, as the potential energy will simultaneously depend on all the remaining variables.

2D-specific partition functions. Returning to Eq. 10 and Eq. 11, the 2D system will differ in several key respects. We now consider both proteins 1 and 2 to be bound to the membrane surface, with the membrane oriented in the x-y plane such that its normal typically points in the z-direction (Figure 1). The integrals over the translational position and orientation of protein 1 in

the volume are now no longer unrestricted in 3D space. The height z_1, the pitch Θ_1, and the roll Φ_1 are limited by the membrane for both proteins. The other three integrals over x_1, y_1, Ψ_1 are unrestrained, and we again can then assert that the potential energy of the system is independent of these variables, reducing to $U(z_1, \Phi_1, \Theta_1, \boldsymbol{r_1}, \boldsymbol{r_2}, \boldsymbol{r_{s,m}}, \boldsymbol{R}_{21}, \boldsymbol{\Omega}_2)$. These integrals can then be immediately integrated to produce:

$$Z_s^{2D} = 2\pi SA \int_0^{Lmem} \mathrm{d}z_1 \int_0^{2\pi} d\Phi_1 \int_0^{\pi} \sin(\Theta_1)\, d\Theta_1 Z_{21,s}^{2D} \#(14)$$

where $SA = L^2$, thus differing from Eq. 12. We have rewritten the integral $\mathrm{d}z_1$ over $Lmem$ to indicate that not all values of z_1 are allowed; the proteins must remain adhered to the membrane to report on a 2D equilibrium constant. We do not need to specify *a priori* the value of $Lmem$, but the fluctuations of the protein in z_1 when bound to the membrane will set the range. If the protein dissociates from the membrane, $z_1 > Lmem$, those configurations should not contribute to the configuration integrals for bound or unbound ensembles. The remaining integrals are:

$$Z_{21,bnd}^{2D} = \int_{A,z_{21}} d\,\boldsymbol{R}_{21} \int d\,\boldsymbol{\Omega}_2 \int d\boldsymbol{r_1} d\boldsymbol{r_2}\, d\boldsymbol{r_{s,m}} H(r_{cut} - |\boldsymbol{R}_{21}|) \exp\left(-\beta U(z_1, \Phi_1, \Theta_1, \boldsymbol{r_1}, \boldsymbol{r_2}, \boldsymbol{r_{s,m}}, \boldsymbol{R}_{21}, \boldsymbol{\Omega}_2)\right) \text{15a}$$

$$Z_{21,unb}^{2D} = \int_{A,z_{21}} d\,\boldsymbol{R}_{21} \int d\,\boldsymbol{\Omega}_2 \int d\boldsymbol{r_1} d\boldsymbol{r}_{s,m} d\boldsymbol{r_2}\, H(|\boldsymbol{R}_{21}| - r_{cut}) \exp\left(-\beta U(z_1, \Phi_1, \Theta_1, \boldsymbol{r_1}, \boldsymbol{r_{s,m}}, \boldsymbol{r_2}, \boldsymbol{R}_{21}, \boldsymbol{\Omega}_2)\right) \quad \text{(15b)}$$

Where we now note that r_{cut} defines the A_{cut} for the bound ensemble, as the height $Lmem$ is already restricted for both ensembles.

II.D Assumptions to simplify the ratio of 2D and 3D partition functions

To estimate the relative dissociation constants of Eq. 9 without having to compute the partition functions across all the remaining variables $\boldsymbol{r_1}, \boldsymbol{r_{s,m}}, \boldsymbol{r_2}, \boldsymbol{R}_{21}, \boldsymbol{\Omega}_2$, (also z_1, Φ_1, Θ_1 in 2D) we proceed with simplifying assumptions.

Simplified 3D partition functions: For the unbound state in 3D, we will assume that the potential energy becomes independent of the relative separation and orientation of the molecules to one another, as those interactions are too long-range and the monomers are thus no longer interacting, so $U(\boldsymbol{r_1}, \boldsymbol{r_2}, \boldsymbol{r_S}) = constant$. From Eq. 11b, we thus integrate over $\boldsymbol{R}_{21}$ and $\boldsymbol{\Omega}_2$ to get a factor of $8\pi^2(V - V_{cut})$, where we subtracted out contributions of states that are sampled in the bound ensemble. For the solvent degrees of freedom, we can assume that it is only the hydration layers that contribute to any free energy difference between the bound and unbound states, with the bulk solvent canceling out. We denote the integral over the bulk water potential energy as C_{bulk}.

$$Z_{21,unb}^{3D} \cong 8\pi^2(V - V_{cut})C_{bulk} \int d\boldsymbol{r_1} d\boldsymbol{r}_{hyd} d\boldsymbol{r_2} \exp\left(-\beta U\left(\boldsymbol{r_1}, \boldsymbol{r_2}, \boldsymbol{r_{hyd}}\right)\right) \#(16)$$

For the bound ensembles in 3D, the only simplifying assumptions are to the bulk solvent degrees of freedom,

$$Z_{21,bnd}^{3D} \cong C_{bulk} \int_0^L dz_{21} \int_0^L dy_{21} \int_0^L dx_{21} \int_0^{2\pi} d\Psi_2 \int_0^{2\pi} d\Phi_2 \int_0^{\pi} \sin(\Theta_2)\, d\Theta_2 \int d\boldsymbol{r_1} d\boldsymbol{r}_{hyd} d\boldsymbol{r_2} \#$$

$$\exp\left(-\beta U\left(\boldsymbol{R}_{21}, \boldsymbol{\Omega}_2, \boldsymbol{r_1}, \boldsymbol{r_2}, \boldsymbol{r_{hyd}}\right)\right) H(r_{cut} - |\boldsymbol{R}_{21}|). \#(17)$$

Simplifications to the 2D partition function: For the unbound state in 2D, we can make similar assumptions, where first we assume that U is independent of the $x_{21} - y_{21}$ separation and protein 2's yaw Ψ_2. We then assume the 'bulk' solvent (both water and membrane) at distance from the protein can be integrated over to give C'_{bulk}.

$$Z_{unb}^{2D} \cong (2\pi)^2 SA(SA - SA_{cut})C'_{bulk} \int_0^{Lmem} \mathrm{d}z_1 \int_0^{2\pi} d\Phi_1 \int_0^{\pi} \sin(\Theta_1)\, d\Theta_1 \int_{Lmem} \mathrm{d}z_{21} \int_0^{2\pi} d\Phi_2 \int_0^{\pi} \sin(\Theta_2)\, d\Theta_2$$

$$\int d\boldsymbol{r_A} d\boldsymbol{r}_{s,m,hyd} d\boldsymbol{r_B} \exp\left(-\beta U\left(z_1, \Phi_1, \Theta_1, z_{21}, \Phi_2, \Theta_2, \boldsymbol{r_1}, \boldsymbol{r_{s,m,hyd}}, \boldsymbol{r_2}\right)\right) \#(18)$$

We now further assume that the potential energy that depends on the height and rigid-body orientations of either protein is independent of the internal coordinates or solvent degrees of freedom.
$U\left(z_1, \Phi_1, \Theta_1, z_{21}, \Phi_2, \Theta_2, \boldsymbol{r_1}, \boldsymbol{r_{s,m,hyd}}, \boldsymbol{r_2}\right) \cong U(z_1, \Phi_1, \Theta_1) + U\left(z_{21}, \Phi_2, \Theta_2\right) + U\left(\boldsymbol{r_1}, \boldsymbol{r_{s,m,hyd}}, \boldsymbol{r_2}\right)$. This gives us:

$$Z_{unb}^{2D} \cong (2\pi)^2 SA(SA - SA_{cut}) C'_{bulk} f_{z_1,\Phi_1,\Theta_1} f_{z_{21},\Phi_2,\Theta_2} \int d\boldsymbol{r_1} d\boldsymbol{r}_{hyd} d\boldsymbol{r_2} \exp\left(-\beta U\left(\boldsymbol{r_1}, \boldsymbol{r_{s,m,hyd}}, \boldsymbol{r_2}\right)\right) \#(19)$$

where

$$f_{z_1,\Phi_1,\Theta_1} = \int_0^{Lmem} \mathrm{d}z_1 \int_0^{2\pi} d\Phi_1 \int_0^{\pi} \sin(\Theta_1)\, d\Theta_1 \exp\left(-\beta U(z_1, \Phi_1, \Theta_1)\right) \#(20)$$

Has units of length via the integral over $\mathrm{d}z_1$, and has the same form for protein 2. The value of f in 2D will be less than the 3D value due to the membrane restrictions, where the potential energy is independent of these coordinates and thus integrates in 3D to $f_{z_1,\Phi_1,\Theta_1} = 4\pi L$. We note that the 2D $U(z_1, \Phi_1, \Theta_1)$ must therefore measure deviations of the potential energy from the 3D $U(z_1, \Phi_1, \Theta_1) \equiv 0$, which can be achieved by setting $\min(U) = 0$.

For the 2D bound state, we will make the same assumption in 3D that the bulk solvent degrees of freedom can be integrated out. We will further assume that the orientation of protein 1 in the box can be assumed largely independent of the other variables, or $U\left(z_1, \Phi_1, \Theta_1\, \boldsymbol{r_1}, \boldsymbol{r_{s,m,hyd}}, \boldsymbol{r_2}, \boldsymbol{R}_{21}, \boldsymbol{\Omega}_2\right) \cong U_b(z_1, \Phi_1, \Theta_1) + U\left(\boldsymbol{r_1}, \boldsymbol{r_{s,m,hyd}}, \boldsymbol{r_2}, \boldsymbol{R}_{21}, \boldsymbol{\Omega}_2\right)$ and where we use the subscript U_b to indicate that the potential energy dependence for protein 1's rigid body orientation in the bound state may be slightly different than in the unbound state. This assumption is not as well-founded for the bound state, as the energy variation with the orientation of protein 2 is likely not independent of protein 1's orientation. Because of the membrane restriction, distinct orientations of 1 and 2 may simultaneously produce different potential energies. Nonetheless, with this simplification:

$$Z_{bnd}^{2D} \cong 2\pi SA\; C'_{bulk} f_{b,z_1,\Phi_1,\Theta_1} \int_0^{Lmem} dz_{21} \int_0^{L} dy_{21} \int_0^{L} dx_{21} \int_0^{2\pi} \mathrm{d}\Psi_2 \int_0^{2\pi} d\Phi_2 \int_0^{\pi} \sin(\Theta_2)\, d\Theta_2$$

$$\int d\boldsymbol{r_A} d\boldsymbol{r}_{s,m} d\boldsymbol{r_B} \exp\left(-\beta U\left(\boldsymbol{r_1}, \boldsymbol{r_{s,m,hyd}}, \boldsymbol{r_2}, \boldsymbol{R}_{21}, \boldsymbol{\Omega}_2\right)\right) H(r_{cut} - |\boldsymbol{R}_{21}|) \#(21)$$

II.E Theoretical expressions for the ratios of 2D and 3D K_D

Returning now to the ratios of the partition functions, in 3D we have from Eq. 16 and 17:

$$\frac{Z_{bnd}{}^{3D}(V)}{Z_{unb}{}^{3D}(V)} = \frac{\int_0^L dz_{21}\int_0^L dy_{21}\int_0^L dx_{21}\int_0^{2\pi} d\Psi_2\int_0^{2\pi} d\Phi_2\int_0^{\pi}\sin(\Theta_2)d\Theta_2\int d\boldsymbol{r_1}d\boldsymbol{r_{hyd}}d\boldsymbol{r_2}\exp\left(-\beta U\left(\boldsymbol{r_1},\boldsymbol{r_{hyd}},\boldsymbol{r_2},\boldsymbol{R}_{21},\boldsymbol{\Omega}_2\right)\right)H(r_{cut}-|\boldsymbol{R}_{21}|)}{8\pi^2(V-V_{cut})\int d\boldsymbol{r_1}d\boldsymbol{r_{hyd}}d\boldsymbol{r_2}\exp\left(-\beta U\left(\boldsymbol{r_1},\boldsymbol{r_{hyd}},\boldsymbol{r_2}\right)\right)} \#(22)$$

.

For the ratio in 2D, we will now also simplify out the membrane degrees of freedom. If we assume that the interface of the proteins to the membrane contributes the same energetically to the bound and the unbound monomers, $U_{bnd}\left(\boldsymbol{r_{m,hyd}}\right) \cong U_{unb}\left(\boldsymbol{r_{m,hyd}}\right)$, then their integrals will cancel in the ratio, producing:

$$\frac{Z_{unb}{}^{2D}}{Z_{bnd}{}^{2D}} = \frac{2\pi(SA-SA_{cut})f_{z_1,\Phi_1,\Theta_1}f_{z_{21},\Phi_2,\Theta_2}\int d\boldsymbol{r_1}d\boldsymbol{r_{hyd}}d\boldsymbol{r_2}\exp\left(-\beta U\left(\boldsymbol{r_1},\boldsymbol{r_{hyd}},\boldsymbol{r_2}\right)\right)}{f_{b,z_1,\Phi_1,\Theta_1}\int_0^{Lmem} dz_{21}\int_0^L dy_{21}\int_0^L dx_{21}\int_0^{2\pi}\mathrm{d}\Psi_2\int_0^{2\pi} d\Phi_2\int_0^{\pi}\sin(\Theta_2)d\Theta_2\int d\boldsymbol{r_1}d\boldsymbol{r_{hyd}}d\boldsymbol{r_2}\exp\left(-\beta U\left(\boldsymbol{r_1},\boldsymbol{r_{hyd}},\boldsymbol{r_2},\boldsymbol{R}_{21},\boldsymbol{\Omega}_2\right)\right)H(r_{cut}-|\boldsymbol{R}}$$

.

Inserting these two ratios into the relative K_D formula of Eq. 9, we will assume the area of volume lost due to the bound state is relatively small compared to the unbound state: $(SA - SA_{cut})/SA \cong 1$ and $V/(V - V_{cut}) \cong 1$ so the dependence on the system size disappears. Currently we therefore have:

$$\frac{K_D{}^{2D}}{K_D{}^{3D}} \cong \frac{f_{z_1,\Phi_1,\Theta_1}f_{z_{21},\Phi_2,\Theta_2}}{4\pi f_{b,z_1,\Phi_1,\Theta_1}}\frac{\int\exp\left(-\beta U\left(\boldsymbol{r_1},\boldsymbol{r_{hyd}},\boldsymbol{r_2}\right)\right)_{2D,unb}\int\exp\left(-\beta U\left(\boldsymbol{r_1},\boldsymbol{r_{hyd}},\boldsymbol{r_2},\ \boldsymbol{R}_{21},\ \boldsymbol{\Omega}_2\right)\right)_{3D,bnd}}{\int\exp\left(-\beta U\left(\boldsymbol{r_1},\boldsymbol{r_{hyd}},\boldsymbol{r_2}\right)\right)_{3D,unb}\int\exp\left(-\beta U\left(\boldsymbol{r_1},\boldsymbol{r_{hyd}},\boldsymbol{r_2},\ \boldsymbol{R}_{21},\ \boldsymbol{\Omega}_2\right)\right)_{2D,bnd}} \#(24)$$

Where we compressed the notation of the integrals from Eq. 22 and 23 to highlight that the potential energies now depend on the same variables in 2D and 3D, with the unbound states depending only on the internal coordinates and hydration solvent, while the bound state also depends on the relative position and orientation of protein 2 in the bound state volume.

This ratio dramatically simplifies if we assert (for now) that the configuration integral of the unbound state is the same in 2D and 3D, and same with the bound states, which we will revisit in Eq. 27-28 below. If we further assume that the potential energy is separable, $U(z_1, \Phi_1, \Theta_1) = U(z_1) + U(\Phi_1) + U(\Theta_1)$, then

$$\zeta_1 = \int_0^{Lmem} \mathrm{d}z_1 \exp\left(-\beta U(z_1)\right) \#(25a)$$

$$f_{\Phi_1} = \int_0^{2\pi} d\Phi_1 \exp\left(-\beta U(\Phi_1)\right) \#(25b)$$

$$f_{\Theta_1} = \int_0^{\pi} \sin(\Theta_1)\, d\Theta_1 \exp\left(-\beta U(\Theta_1)\right) \#(25c)$$

And Eq. 24 becomes

$$\frac{{K_D}^{2D}}{{K_D}^{3D}} \approx \frac{\zeta_1 f_{\Phi_1} f_{\Theta_1} \zeta_{21} f_{\Phi_2} f_{\Theta_2}}{\zeta_{b,1} f_{b,\Phi_1} f_{b,\Theta_1} 4\pi} \approx \frac{\zeta_{21} f_{\Phi_2} f_{\Theta_2}}{4\pi} \#(26)$$

Eq. 26 is the same as the result found in previous work[16, 41] that characterized 2D binding for rigid domains, where the focus was on binding between adhesion receptors across a cell-cell membrane gap, rather than the peripheral membrane proteins studied here. As noted above, the values in Eq. 26 will be less than the 3D values, $\zeta_1 < L$, $f_{\Phi_1} < 2\pi$, and $f_{\Theta_1} < 2$, where the comparison with 3D requires setting all potentials in Eq. 25 to have a minimum value of $U = 0$. If the restraints on protein 1 are comparable in the unbound and bound ensemble, which is feasible for two proteins on the same membrane, then we get the final expression on the right in Eq. 26. In this rigid-body limit, the 2D relative to 3D dissociation constant is a lengthscale that is determined by the z fluctuations when membrane bound, multiplied by the fractional loss in pitch and roll angles.

Generalizing from the rigid-body approximation

Proteins are not truly rigid, and one assumption of the simplifications to reach Eq. 26 is that there is no change in configurational entropy at the backbone or residue level from 3D to 2D. For the unbound state, we assumed that the configurations accessible to both monomers in Eq. 24, $\int d\boldsymbol{r_1} d\boldsymbol{r}_{hyd} d\boldsymbol{r_2} \exp\left(-\beta U\left(\boldsymbol{r_1}, \boldsymbol{r_{hyd}}, \boldsymbol{r_2}\right)\right)$, are the same whether they are solvated in 3D, or bound in 2D to the membrane, given a matching rigid-body orientation. However, for proteins that form a significant interface with the membrane, like the peripheral membrane proteins we study here, the inherent flexibility of the backbone and residues could be reduced via surface localization, beyond the rigid-body restrictions we have accounted for already. This change in flexibility would always reduce the range over which the integrals are evaluated in the 2D state, such that the scalar ratio in Eq. 24 is no longer 1, but is:

$$\frac{\int \exp\left(-\beta U\left(\boldsymbol{r_1}, \boldsymbol{r_{hyd}}, \boldsymbol{r_2}\right)\right)_{2D,unb}}{\int \exp\left(-\beta U\left(\boldsymbol{r_1}, \boldsymbol{r_{hyd}}, \boldsymbol{r_2}\right)\right)_{3D,unb}} \leq 1 \#(27)$$

Where we assumed that the potential energy across these equivalent degrees of freedom are the same. We note that the replacement of the water interface with the membrane interface was cancelled out when comparing the bound to unbound ensemble.

For the bound ensemble, two issues could impact our assumption of equivalent configuration integrals. One is the same as that mentioned above, that binding to the membrane restricts the configurations accessible to backbone and side-chain atoms relative to the 3D bound state. This results in a corresponding increase in the scalar ratio of Eq. 24:

$$\frac{\int \exp\left(-\beta U\left(\boldsymbol{r_1}, \boldsymbol{r_{hyd}}, \boldsymbol{r_2}, \boldsymbol{R}_{21}, \boldsymbol{\Omega}_2\right)\right)_{3D,bnd}}{\int \exp\left(-\beta U\left(\boldsymbol{r_1}, \boldsymbol{r_{hyd}}, \boldsymbol{r_2}, \boldsymbol{R}_{21}, \boldsymbol{\Omega}_2\right)\right)_{2D,bnd}} \geq 1 \#(28)$$

A further assumption made above is that the (dominant) bound state configurations are the same in 3D and 2D. We know for a fact that the configurational space is distinct for the above integrals in Eq. 28, as both $\boldsymbol{R}_{21}$ and $\boldsymbol{\Omega}_2$ have reduced sampling in 2D via z_{21}, Θ_2, Φ_2. However, if the bound state contains a narrow set of structures with sufficiently low potential energy that are equally accessible in both 3D and 2D, then the Boltzmann weight of those configurations will dominate, rendering all other configurations, including those 'lost' in 2D, negligible, such that $\int \exp\left(-\beta U\left(\boldsymbol{r_1}, \boldsymbol{r_{hyd}}, \boldsymbol{r_2}, \boldsymbol{R}_{21}, \boldsymbol{\Omega}_2\right)\right)_{3D,bnd} \approx \exp\left(-\beta U_{min}\right)$ also holds in 2D. This assumption is less accurate if a large variety of nonspecific states contribute to the bound state configuration integral. Overall, if all configurations that are sampled in 2D are also sampled in 3D, these two equations both emphasize that the 3D integrals will always be at least as big as their 2D counterparts, because $\exp(-\beta U)$ is always positive, and 3D can access additional configurations.

Critically, we note that these comparisons assume that the configurations sampled in both 2D and 3D have comparable values of (relative) potential energy. However, if the protein undergoes a conformational change upon membrane binding in either bound or unbound states, it could sample a different range of potential energies. If the potential energies lower in the 2D ensembles due to such significant conformational changes, then neither of these inequalities in Eq. 27 or 28 need hold, and the configurational integrals could instead increase in magnitude in 2D relative to 3D.

III. METHODS

III.A Molecular Dynamics Simulations

System Setup: We performed MD simulations with three different system environments, (a) solvated and freely diffusing proteins, (b) proteins bound to a membrane and (c) fully solvated proteins with translational and rotational motion restricted to a 2D 'pseudo' membrane (see Figure 1). All three environments were simulated using the newly parametrized MARTINI 3.0[42] and the first two were also simulated using the MARTINI 2.0 forcefield, using the GROMACS package (version 2021.4 for MARTINI 3.0 and 2020.2 for MARTINI 2.0). All systems were simulated using metadynamics (aside from equilibration and a few short unbiased trajectories) using the PLUMED plugin (version 2.8.0). The structure for LSP1 was obtained from the PDB database (accession code: 3PLT). Two copies of chain A were used for the homodimer since chain B had missing residues. The LSP1 homodimer was coarse grained with the ELNEDIN elastic network (spring force constant 500 kJ mol^{-1} nm^{-2} and cutoff as 0.9nm) using the *martinize.py* tool downloaded with the open beta version 3.0.b.3.2, followed by correction of side chain dihedrals as recommended using the *bbsc.sh* script.

For the solution simulations, the initial configuration of the two monomers are in their bound state, as extracted from the crystal structure. The proteins are solvated using the standard water model with 0.1M of NaCl in a simulation box of ~ 36 x 36 x 36 nm^3 under periodic boundary conditions. Energy minimization was performed which was followed by 5 ns of equilibration in the NVT ensemble and an additional 5 ns of equilibration in the NPT ensemble for our MARTINI 3 models and as previously described for our solution MARTINI 2 simulations. The relatively large box size was used to ensure that for these dimerization simulation studies, proteins oriented in an end-to-end fashion would not be able to simultaneously interact with their physical partner at one end and the periodic image of the same protein at their other end, as that would mimic a filament and not a dimer.

For membrane simulations, the LSP1 dimer was added to an equilibrated bilayer in a box of size ~ 38 x 38 x 19 nm^3.The phospholipid bilayer was setup using the *insane.py* tool (modified for martini 3 lipids) with a composition of 80% DOPC, 10% POPS and 10% POP6, which is the MARTINI name for PIP_2. The bilayer was first neutralized and solvated with the standard water model and 0.1 M NaCl followed by a similar protocol of minimization and equilibration runs. The LSP1 monomers in the bound dimer form (like seen in the PDB structure) were then added to

the equilibrated bilayer and positioned such that its membrane binding residues face the membrane. After adding the protein, the system was again minimized and equilibrated following the same protocol. For membrane simulations with MARTINI2 we followed these same steps from the beginning, except of course swapping out the force-field topology and molecule parameter file (bead names).

For the pseudo-membrane system we use a simulation volume of ~ 37.0 x 37.0 x 37.0 nm^3. The system was set up using a configuration of the two MARTINI LSP1 monomers present in the bound state, at the end of a short unbiased simulation on the membrane surface. The dimer was then isolated and solvated with the standard water model and 0.1 M NaCl. First the system was energy minimized, then equilibrated using 5ns NVT, followed by 5ns NPT. We then introduced our harmonic restraint potentials to both monomers in a stepwise manner. The three harmonic restraint potentials over the height z_{surf}, and two orientational angles θ and ϕ are detailed below. They were switched on in the order $U(z_{\mathrm{surf}}), U(\theta), U(\phi)$ over a period of 1400ns, and kept on for the remainder of the simulations. To switch them on, we started off with a low or 'soft' force constant, letting it adjust to each restriction before ramping up the force constant to its final target value. The simulation parameters were otherwise the same as the other system environments.

Simulation parameters: All simulations were performed using improved MARTINI parameters[43]. The electrostatic interactions were modeled using the Reaction-field method with a 1.1 nm cutoff. The dielectric constant was set to default value of 15 with an $\varepsilon_{rf} = \infty$. The Lennard-Jones potential was used with a 'vdw-modifier' to smoothly shift to zero after a cutoff of 1.1 nm. We used the leapfrog integrator with a timestep of 20 fs. Neighbor lists were constructed using the Verlet scheme with nstlist set to 10 and the Verlet-buffer-tolerance (VBT) was kept at the default value of 0.005 kJ mol^{-1} ps^{-1}. However, these default parameters were shown to contribute to artifacts in the pressure tensor leading to unphysical undulations in the membrane as reported by Kim et al. 2023. While we did not observe any unphysical characteristics in our system, we altered the VBT parameter to 0.0002 kJ mol^{-1} ps^{-1} after 156 µs for MARTINI 3.0, as per their recommendation. The temperature was maintained at 310 K using the velocity rescaling thermostat while the pressure was maintained at 1 bar (semi-isotropic for membrane simulations) using a Berendsen barostat for equilibration (coupling constant of 5.0 bar^{-1}) and a Parinello-Rahman barostat of 12.0 bar^{-1} for the production runs.

Establishing constraints for a 2D 'pseudomembrane' system. In our pseudomembrane simulations, the LSP1 monomers are simulated fully solvent in a 3D environment, without any

membrane. However, of the 3 translational and 3 rotational rigid-body orientational axes for rotation, we introduce constraints on 3 of them: translational diffusion in the z-direction, and rotational motion of the pitch around the long (q) and short (f) axis of both monomers. Translational diffusion in x and y are unconstrained, as is rotation about the z-axis, or the effective yaw angle, as both proteins and lipids diffuse. These constraints capture the impact of the membrane on these rigid-body dynamics of the protein. We parameterized the constraints on each of these three variables by quantifying the observed values that are sampled when our proteins are bound to an actual membrane (Figure S1,2).

For all three variables, we collected data from unbiased simulations of almost 1 μs of the two LSP1 monomers bound to the lipid membrane (Figure S1,2). The monomers were bound into the dimer state for the full trajectory, although statistics collected on unbound monomers were not substantially different. For the translational motion we defined a position on the protein via all residues that participate in the membrane binding patch, 56ARG,63LYS,66LYS,70ARG,126ARG, 130LYS,133ARG, and measured the center-of-geometry which can be denoted as $\boldsymbol{r}_{patch} = [x_{patch,} y_{patch,} z_{patch}]$. For generating the probability distributions of z_{surf}, we first selected all lipid headgroups which were within of 1.2 nm from any of the residues in the membrane binding patch, and measured the center-of-geometry, which can be denoted as $r_{Mpatch} = [x_{Mpatch}, y_{Mpatch}, z_{Mpatch}]$. z_{surf} was then evaluated as $z_{\mathrm{surf}} = z_{patch} - z_{Mpatch}$. However, to accurately sample the fluctuations of the protein in the z-dimension, which is crucial for evaluating the integral in Eq 25a, we have to measure the separation of the protein as a whole from the membrane. To do so, we calculate z_{disp}, which is given as $z_{disp} = z_{cogP} - z_{lipid}$. Here z_{cogP} is the center-of-geometry of the protein monomer denoted by - $r_{cogP} = [x_{cogP}, y_{cogP}, z_{cogP}]$, and z_{lipid} is the coordinate of a single lipid located at the same position as x_{cogP}, y_{cogP}. We calculate z_{disp} for the lipid on the outer and the inner leaflet, for comparison.

We generate a probability density function $p_{mem}(z_{\mathrm{surf}})$ from the sampled z_{surf} values and transforms it to a potential of mean force via:

$$U(z_{\mathrm{surf}}) = -k_B T \log\big(p_{mem}(z_{\mathrm{surf}})\big) \qquad (30)$$

The distribution and potential are shown in Fig. S1. The simplest potential is a harmonic potential, and thus we fit our sampled $U(z_{\mathrm{surf}})$ curve to:

$$U(z_{\mathrm{surf}}) = \frac{1}{2} k_z \, (z_{\mathrm{surf}} - z_0)^2 + cons \qquad (31)$$

Where k_z is the spring constant in units of kJ/mol/nm2 and z_0 is the average separation sampled in the simulations. The constant is to constrain the potential to the normalized probability distribution, such that $cons = \frac{k_B T}{2} \ln\left(\frac{2\pi k_B T}{k_z}\right)$. Fitting the simulation data to the harmonic potential produced a best-fit k_z =167 kJ/mol/nm^2 and z_0 = 1.11 nm for chain A and k_z =160 kJ/mol/nm^2 , z_0 = 1.32 nm for chain B.

To quantify the sampling of the orientations of each monomer, we define a vector $\vec{r}_{\text{long}}$ connecting beads 84LYS to 150 THR along the long-axis of the monomer. We measure the orientation of this vector relative to the global z-axis as a measure of pitch, $\theta = \text{acos}\left(\frac{\vec{r}_{\text{long}}}{\|\vec{r}_{\text{long}}\|} \cdot \begin{bmatrix}0\\0\\1\end{bmatrix}\right)$. To quantify the sampling relative to another (nearly) orthogonal axis, we define a vector $\vec{r}_{\text{short}}$ connecting beads 259GLU to 80ARG along the short-axis of the monomer. Similar to the pitch θ, we again compute the vector orientation relative to the global z-axis via $\phi = \text{acos}\left(\frac{\vec{r}_{\text{short}}}{\|\vec{r}_{\text{short}}\|} \cdot \begin{bmatrix}0\\0\\1\end{bmatrix}\right)$. These angles are straightforward to calculate for performing restraints during our pseudomembrane simulations, both ranging over $[0, \pi]$. However, we note that for theoretical comparisons, they do not represent two Euler angles for rigid body rotation, and in the analysis section below we define the calculation of Euler angles for our monomers.

As for the z separation, we can transform the probability distributions we collect for each of these orientational variables θ and ϕ to potentials of mean force. As shown in Fig S1, these potentials are relatively well fit by harmonic potentials of the same form as above. We separately fit the distribution for each monomer, with values collected in Table S1. The spring force constant for the θ angle is 401 kJ/mol/rad^2 with the mean value at 1.55 rad for chain A and 550 kJ/mol/rad^2 for chain B with a 1.48 mean value. For the ϕ orientation, the force constant was 121 kJ/mol/rad^2 with the mean value being 0.46 rad for chain A and for chain B, the force constant was 106 kJ/mol/rad^2 with a mean value of 0.39 rad.

Metadynamics Parameters: For building the free energy surface (FES), we first used the standard metadynamics technique (https://doi.org/10.1073/pnas.202427399) and later we switched on the well-tempered bias (10.1103/PhysRevLett.100.020603) to help with convergence. The FES was evaluated with respect to two collective variables (CVs), d_1 and d_2, representing distances between two pairs of sites that are in contact in the bound crystal

structure. Both variables are illustrated in Fig 1. The first collective variable d_1 is the distance between the center of geometry of two sites comprised of residues 57LYS-64THR on chain A and residues 78GLU-92ASP on chain B. The second collective variable $d_2$is the distance between the sites consisting of residues 224LEU-229ASP on chain A and residues 189ASN-196LYS.

To briefly explain the parameters defined for a metadynamics simulation, we define the bias potential here. The bias potential is a function of the CVs, $\vec{s} \epsilon \{d_1, d_2\}$ and time t, and is expressed as a sum over deposited Gaussian potentials:

$$V(\vec{s}, t) = \sum_{t=\tau_G, 2\tau_G, \ldots}^{t_F} w\, e^{\left(-\frac{(s_1 - d_1(t))^2}{2{\sigma_1}^2}\right)} e^{\left(-\frac{(s_2 - d_2(t))^2}{2{\sigma_2}^2}\right)} \qquad (32)$$

Here w is the height of the Gaussian potential in kJ/mol, $d_1(t)$ and $d_2(t)$ represent the instantaneous value of the CVs at time t, $\tau_G$is the deposition time of the Gaussian potential, and σ_1 and σ_2 are the widths of the Gaussians in the dimension of each CV. After a sufficient long time t_F, the free energy $F(\vec{s})$ can be evaluated from the bias potential to with a constant offset:

Write out the equations for the FES with and without the well-tempered bias.

$$F(\vec{s}) = -V(\vec{s}, t \rightarrow \infty) + C \qquad (33)$$

In the well-tempered version, the height of the deposited Gaussian potential is scaled down by a factor of $e^{\frac{-V(\vec{s},t)}{k_B \Delta T}}$, where ΔT is defined based on the bias factor $\gamma = \frac{T + \Delta T}{T}$. Here γ is called the bias factor which is the ratio of the effective sampling temperature of the CVs to the system temperature. This means that in regions where larger biases have accumulated, the height of the newer bias potentials is smaller. The FES in the long-time limit is then estimated as –

$$F(\vec{s}) = -\frac{\gamma}{\gamma - 1} V(\vec{s}, t \rightarrow \infty) + C_1 \qquad (34)$$

In our simulations, we estimate the FES from the standard metadynamics part of the simulation (F_{stm}) using Eq 33, and the well-tempered part of the simulation (F_{wtm}) using Eq 34 and then add the corresponding contributions to compute the final FES. For the solution simulations, the widths of the Gaussian potentials used w.r.t each CV was $\sigma_1 = \sigma_2 = 0.1$nm. The height was initially, w=5 kJ/mol, but was reduced to 1 kJ/mol after 28us, to better refine the FES. We switched to well-tempered metadynamics after 106 µs, which allows the height w of the barriers

to decrease to converge the FES, γ =80. The choice of τ_G is ideally long enough that the CVs equilibrate from the previously deposited Gaussian. This makes it coupled to the Gaussian widths, as the system should have time to sample away from the bias before another Gaussian is deposited. We calculated the relaxation time of our CVs to travel this distance σ_1 as ~280 ps and used $\tau_G = 280ps$.

For the membrane simulations, the relaxation time along the CVs is slowed relative to solution due to the reduced diffusion of the proteins on the lipid bilayer. To maintain a relatively frequent deposition time of $\tau_G = 300ps$, we therefore had to reduce the widths of our Gaussians to $\sigma_1 = \sigma_2 = 0.04$nm . Initially we used a height of w=5 kJ/mol, but this was reduced to 1 kJ/mol after 96 µs . We switched to well-tempered metadynamics with the bias factor $\gamma = 20$ starting at 156µs . Over the course of the simulation we observed that the well-tempered metadynamics was slowing the sampling of the CV space and thus the convergence. We therefore turned off the well-tempered deposition and resumed the standard version with a height of w=2 kJ/mol after 201 µs.

For the pseudo-membrane simulations, the deposition time used was maintained at 300 ps , while using a slightly larger width of 0.05nm. The Gaussian height was initially set to 5kJ/mol, which was then reduced to 1kJ/mol after 12 us. The well-tempered version was switched on after 18 µs with $\gamma = 20$ until 102 µs after which we resumed the standard version with height of w=1 kJ/mol

Wall potential: To accelerate sampling in our two CVs d_1 and d_2, we introduced a restraint potential at that limits the upper bound value for each CV during the simulation. The restraint wall potential is of the form –

$$W_i = \begin{cases} k_i * (s_i(t) - s_0)^2 & when \quad s_i(t) > s_0 \\ 0 & when \quad s_i(t) \leq s_0 \end{cases}$$

where i =1,2 corresponding to d_1 and d_2. The value of the spring constant k_i was set to 500 kJ mol^{-1} nm^{-2} .The value of s_0 was 21.0 nm for the solution simulations and 19.0 nm for the 2D simulations. We could not simply reduce the box-size because this could introduce artifacts from a monomer interacting with a partner and its periodic image. The restraint potentials were applied using plumed.

III.B Analysis of MD simulations

Evaluating binding free energy from metadynamics simulations: From our metadynamics simulations, we compute the free energy surface $\mathrm{F}(\mathrm{d}_1, \mathrm{d}_2)$ from the deposited hills using Eq. above, combining the FES from the standard and well-tempered parts of the trajectory. This FES is related to the canonical partition function $\mathrm{Z}(\mathrm{d}_1, \mathrm{d}_2)$ via[17]

$$Z(d_1, d_2) = C' \exp\left(-\frac{F(d_1, d_2)}{k_B T}\right)$$

Where C' is a constant. To compute the relative free energy of the bound to the unbound state, we must integrate over this partition function for values of d_1, d_2 that reside in the bound ensemble, vs those in the unbound ensemble. We use a cutoff r_{cut} in both values of the CV to partition the surface into the bound and unbound ensemble. We demonstrate in Fig SX that the ratio converges with a large enough value of r_{cut} . Smaller cutoff values can leave low-energy states in the unbound ensemble; due to the Boltzmann weighting, this misrepresents the relative unbound state free energy. We use numerical integration over both CVs via

$$Z_{bound} = C' \sum_{d_1 < r_{cut}} \sum_{d_2 < r_{cut}} e^{-(F(d_1,d_2)/k_B T} \Delta d_1 \Delta d_2 \qquad \text{Eq (8)}$$

$$Z_{unbound} = C' \sum_{r_{cut} < d_1 < R_{max}} \sum_{r_{cut} < d_1 < R_{max}} e^{-(F(d_1,d_2)/k_B T} \Delta d_1 \Delta d_2 \qquad \text{Eq (9)}$$

Where R_{max} is the maximal separation of the CV in our system, which is limited by the restraining wall we use. This establishes the maximal volume of the unbound ensemble. The constant C' will cancel when taking the ratio. We note that no Jacobian factors are needed for these integrals, despite depending on a radial separation. This is because the FES is computed based on integrating over all microscopic degrees of freedom r^N, with configurations binned based on their value of d_1, d_2, or formally,

$$Z(d_1, d_2) = \int \delta\left(d_1 - d_1(r^N)\right)\delta\left(d_2 - d_2(r^N)\right) exp\left(-\beta U(r^N)\right) dr^N \quad (12)$$

Regions in CV space with larger phase space volume thus contribute more sampled configurations and include the Jacobian weights.

From these partition functions, we can then use the same equations above to quantify the binding free energy and then the dissociation constant, using

$$K_D^{3D} = V^{-1} \exp\left(\frac{\Delta G(V)}{k_B T}\right)$$

Where V is the volume sampled over when computing configurations that contribute to the partition function, $V = 4/3\pi(R_{max}^3 - r_{cut}^3)$

Evaluating convergence of the FES and binding free energy: For evaluating the convergence of FES we show progression of FES at 50%, 80%, 90% completion (Fig S3). To compare the free energy differences between different systems and obtain error estimates, we performed block averaging. The free energy difference was calculated as the mean $\langle \Delta G_i \rangle$ over 'i' blocks where the first block consists of ΔG evaluated at 50% completion of the total simulation time and the subsequent 50% of the simulation divided into 'i-1' blocks. We evaluated the error estimates (ϵ) obtained by considering a 95% CI by using the following expression as given in –

$$\varepsilon = \Phi^{-1}(0.975)\sqrt{\frac{1}{N\,(N-1)}\sum_i^N(\Delta G_i - \langle \Delta G \rangle)^2}$$

We evaluated the error by considering different block sizes for each simulation as shown in SI. For the final free energy estimates, we used a block size of 20 µs for 3D MARTINI 3 and MARTINI 2 simulations. For all 2D simulations a larger block size of 40 µs was used. These estimates are reported in Table 1 along with the instantaneous value $\Delta G_{t=t_{end}}$ which corresponds to the free energy difference computed at the end of the simulation.

Measuring Euler/Tait-Bryan angles for our monomers: Given the long and short axes of our monomer m at any point in time, $\vec{r}_{\text{long}}$ and $\vec{r}_{\text{short}}$, we can define a right-hand orthogonal frame with unit vectors where $\hat{x}_m = \vec{r}_{\text{long}}/\|\vec{r}_{\text{long}}\|$ is the so-called roll axis, $\hat{y}_m = \vec{r}_{\text{short}} \times \hat{x}_m/\|\vec{r}_{\text{short}} \times \hat{x}_m\|$ is the pitch axis, and $\hat{z}_m = \hat{x}_m \times \hat{y}_m$ is the yaw axis (does this need normalization or it is already 1?). We follow the Tait-Bryan angles for intrinsic rotations around the global frame z, y', and x'', where primes indicate rotated frames. We can thus compute

$$\Psi = \arctan\left(\frac{\hat{x}_{m,2}}{\hat{x}_{m,1}}\right)$$

$$\Theta = \arcsin\,(-\hat{x}_{m,3})$$

$$\Phi = \arctan\,(\frac{\hat{y}_{m,3}}{\hat{z}_{m,3}})$$

For yaw (Ψ), pitch (Θ) and roll (Φ), where the subscript indicates the vector index. We computed distributions of sampled values for these angles in both the bound and unbound ensembles. This is needed to approximately predict the ratio of 2D to 3D dissociation constants.

Measuring the height variations of membrane bound proteins: We evaluated the fluctuations in z in multiple ways, in addition to the restrained potentials above. We evaluated the z coordinate of the monomer center-of-mass, and at that same position in x,y, we measured the z position of the lipid on the upper and lower leaflet.

Calculating ensemble averages of potential energies: We computed potential energies of both bound and unbound ensembles. To calculate $\langle U \rangle_x$ from an unbiased equilibrium NPT trajectory, we exploit the ergodic principle to take a simple unweighted time average over configurations within each grid point, $U(\vec{s}) = \frac{\sum_{t=1}^{Nt} U(r^N(t))\delta\left(\vec{s}-\vec{s}(r^N(t))\right)}{\sum_{t=1}^{Nt} \delta\left(\vec{s}-\vec{s}(r^N(t))\right)}$, where *Nt* is the total number of configurations from a trajectory. However, to compute ensemble averages from a biased metadynamics trajectory, we must apply a reweighting factor as we average[44]. We use normalized weights,

$$U(\vec{s}) = \frac{\sum_{t=1}^{Nt} U(r^N(t))\delta\left(\vec{s}-\vec{s}(r^N(t))\right)\exp\left(\beta\left[V\left(s(r^N(t)),t\right)-C(t)\right]\right)}{Q_s}$$

$$Q_s = \sum_{t=1}^{Nt} \delta\left(\vec{s}-\vec{s}(r^N(t))\right)\exp\left(\beta\left[V(s(r^N(t)),t)-C(t)\right]\right),$$

where $C(t)$ is the time-dependent offset[44] and is calculated using the PLUMED plugin. The potential energy averaged over multiple grid points is given by:

$$\langle U \rangle_x = \frac{\sum_{s_i \in x} U(\vec{s}_i) Q_{s_i}}{\sum_{s_i \in x} Q_{s_i}}$$

Normalization reduces numerical issues due to very large values of $V(s(r^N(t)),t) - C(t)$.

Calculating RMSD values over each trajectory: For characterizing the system in terms of its deviation from the crystal structure we use two types of RMSD measurements. To evaluate the conformational changes in each monomer, we calculate the RMSD value of every frame of the trajectory by superimposing each monomer separately onto its crystal counterpart. This removes the translational and rotational degrees of freedom and then the RMSD is calculated by

$$RMSD\left(m_j\right) = \sqrt{\frac{1}{n}\sum_{i=1}^{n}\left|r_i - r_i^{cry\ (m_j)}\right|^2}$$

Where $j = 1,2$ for each monomer, n is the number of atoms and r_i , $r_i^{cry\ (m_j)}$ are the positions of the corresponding atoms in the simulation and crystal structure respectively.

We also calculate $dRMSD$ to assess the dimer configurational states sampled over the course of a simulation. This value is calculated by first superimposing monomer 1 to its crystal counterpart. The $dRMSD$ value is then evaluated by calculating the deviation of monomer 2 w.r.t it's crystal coordinates –

$$dRMSD = \sqrt{\frac{1}{n}\sum_{i=1}^{n}\left|r_i - r_i^{cry\ (m_{j=2})}\right|^2}$$

III.C Rigid-body approximation to K_D^{2D}/K_D^{3D} from simulation data

From Eq 26 above, we can estimate the ratio of 2D to 3D dissociation constants by assuming our proteins are rigid, and measuring the change in sampling of the roll, pitch, and height variables on the membrane. If we assume that each of these potential functions are harmonic in their variable, and we assume the integrals can be extended to +/- infinity,

$$\zeta_1 = \int_0^z e^{-\left(\frac{1}{2k_BT}k_Z(z-z_0)^2\right)}\,dz \cong \sqrt{\frac{2\pi k_BT}{k_Z}}$$

$$f_{\Theta_1} = \int_0^{\pi}\sin(\Theta_1)\,d\Theta_1\exp\left(-\beta k_\theta\left(\Theta_1 - \Theta_{1,0}\right)^2/2\right) \cong k_BT\,/k_\Theta$$

$$f_{\Phi_1} = \int_0^{2\pi} e^{-\left(\frac{1}{2k_BT}k_\phi\left(\Phi_1-\Phi_{1,0}\right)^2\right)}\,d\Phi_1 \cong \sqrt{\frac{2\pi k_BT}{k_\phi}}$$

These potentials can also simply be numerically integrated without assuming any specific functional form, but the above approximations give a sense of how the values vary with the force constants. For each variable, we computed $U(\Phi_1)$ numerically based on determining the probability distribution of observed Φ_1 values via histogramming, and using $U(\Phi_1) = -k_BT\ln(p(\Phi))$, with enforced $\min\left(U(\Phi_1)\right) = 0$.

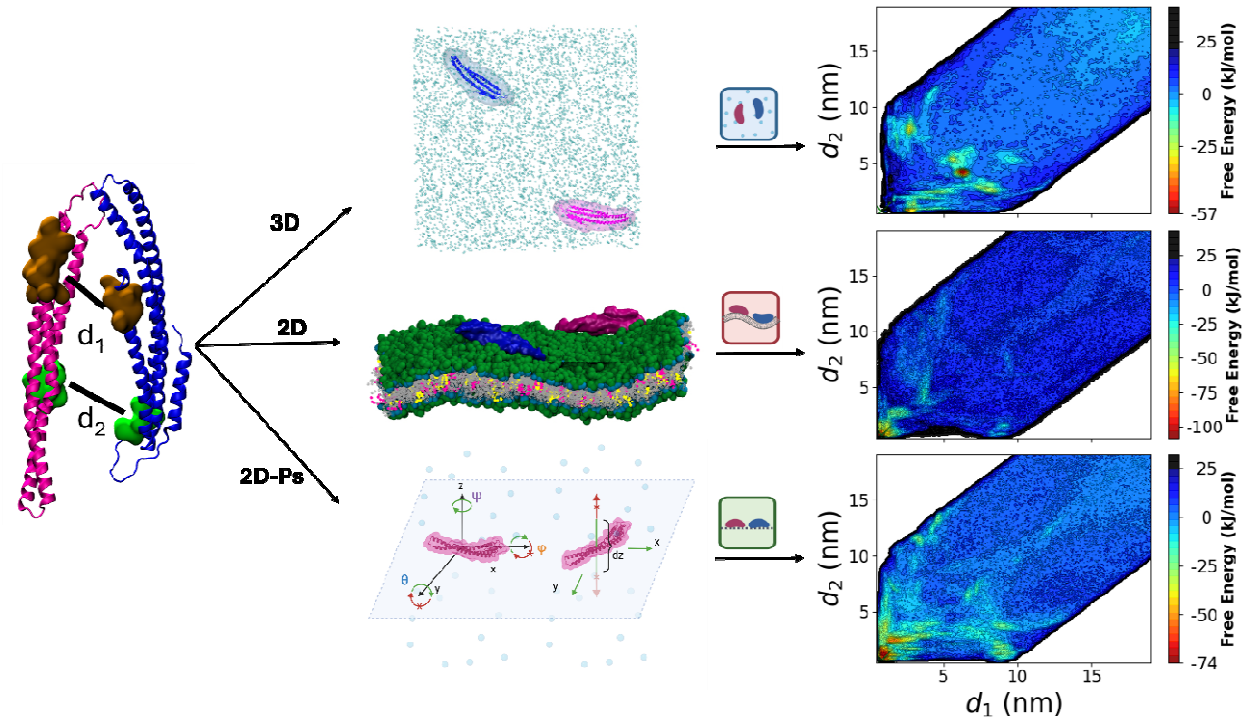

Figure 1 Summary of the simulations performed On the left is shown an LSP1 BAR homodimer representation with the metadynamics collective variables d_1, d_2. The dimerization process is evaluated in 3 different environments – solution (3D), membrane (2D) and a pseudo-membrane 2D plane (2D-Ps) enforced by geometrical restraints. The geometrical restraints are applied to restrict the each protein chain's translational and orientational degrees of freedom as shown. For each environment we performed a single long MD simulation with enhanced sampling to build the free energy surface w.r.t to the collective variables. The binding affinities are then obtained by integrating the FES (right panel) for the respective configurational states. The FES are shown for the MARTINI 3 simulations.

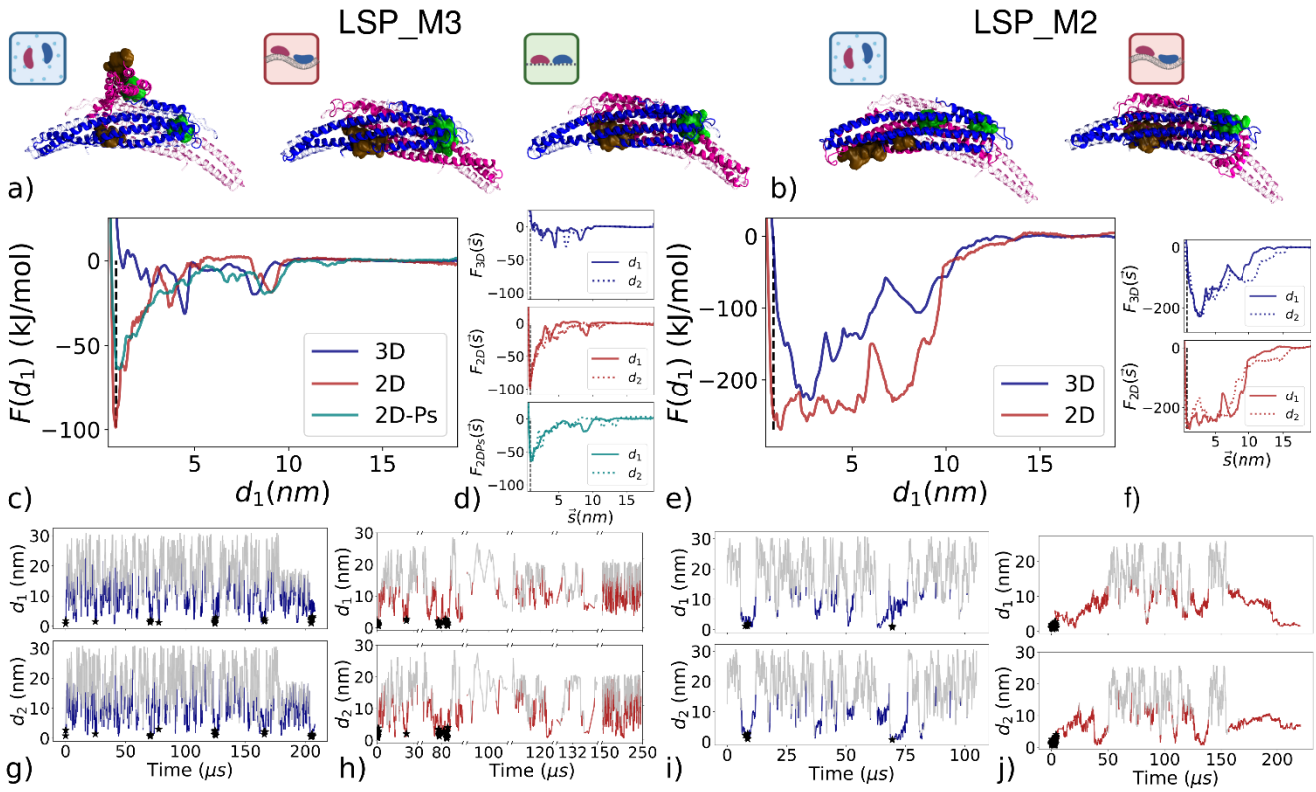

Figure 2 Characterization of the collective variables (CVs) d_1 and d_2 in 3D and 2D for MARTINI3 (LSP_M3) and MARTINI 2 (LSP_M2). The most stable structure in each environment, corresponding to the minimum free energy is shown as an atomistic representation of the two monomers obtained from backmapping the coarse grained structures for **a)** MARTINI 3 and **b)** MARTINI 2. The structures are represented after aligning a single monomer chain (blue) to it's crystal counterpart. For reference the crystal structure of the second chain (magenta) is also shown (magenta glass bubble). **c)** 1-dimensional Free Energy surface w.r.t to d_1 , obtained by integrating the free energy over d_2, shows that the crystal structure (denoted by dashed black line) is the most stable state in 2D membrane and 2D-Ps. The most stable state in 3D corresponds to a non-specifically bound dimer state as seen in a). **d)** 1-dimensional FES plotted w.r.t to both CVs d_1 and d_2 show similar deep energy wells for the crystal structure in 2D membrane and 2D-Ps unlike dimerization in 3D. **e)** 1-dimensional FES for MARTINI2 simulations shows broad and deep energy wells for both 3D and 2D simulations. The most stable state in 2D is closer to the crystal structure than in 3D. However, there are several stable non-specifically bound states in both environments. **f)** 1-dimensional FES plotted w.r.t to both CVs d_1 and d_2 for MARTINI 2. Time evolution of the CVs d_1 (top panel) and d_2 (bottom panel) plotted every 100 ns **g)** 3D (blue) and **h)** 2D (red) in MARTINI 3. There are multiple transitions from the unbound state (gray; d_1, d_2 > 13.0 nm) to the bound state (colored; d_1 and d_2

< 13.0 nm) with some of them also sampling the crystal state (denoted by black stars; dRMSD < 2.0 nm). Similar plots for MARTINI 2 simulations are also shown for **i)** 3D (blue) and **j)** 2D (red). The MARTINI 2 simulations observe multiple transitions from the bound to unbound state but fewer sampling of the crystal state. For the 2D membrane simulations in MARTIN 3, time points which include one of the protein monomers unbound to the membrane are not represented since we do not consider those timepoints in our calculations. The timepoints which are not included are - (33–66 µs, 95.2- 97.8 µs, 101.9-103.3 µs, 127.6-128.5 µs and 138-141 µs) are represented by disjointed segments in the x-axis.

IV. RESULTS

IV.A The free energy surface for binding in 2D is distinct from 3D and better selects the crystal state

We constructed the free energy surface (FES) for a pair of LSP1 monomers in three distinct environments in MARTINI 3: solution (3D), bound to a lipid membrane bilayer (2D), and restricted to sampling on a 2D 'pseudo-membrane' while fully solvated in water (Fig 1). We also computed the FES in MARTINI 2 for 3D solution and 2D membrane environments. The FES was constructed using enhanced sampling via metadynamics (Methods), revealing that LSP1 dimer has distinct behaviors in the two forcefields. In MARTINI 3, the bound states, and particularly the crystal structure configuration, are significantly more favorable in the 2D membrane and pseudomembrane environments (Fig. 1 and 2). In all three environments, our sampling produced many transitions between the bound and unbound states, and at least 2 or more transitions to the crystal structure (Fig. 2g,h and Fig S4). The LSP1 dimerization in 3D in MARTINI 2 is of similar stability as on 2D membrane when considering the complete ensemble of bound states. In both environments while the simulations transition multiple times to the bound state from the unbound, transitions to the crystal state are fewer (Fig 2i,j).

The FES of dimerization in 3D for both MARTINI 3 and MARTINI 2 show that while the bound ensemble is more stable than the unbound ensemble, as expected, the stability is driven by multiple distinct structures that deviate significantly from the crystal structure (Fig 2a,b). In 3D MARTINI 3, while we note that the crystal structure is visited in solution, the monomers depart rapidly from this state, indicating that it does not require any significant force to dissociate it (Fig 2g). The presence of membrane or restriction to a pseudo-membrane in MARTINI 3 decreases the stability of non-specifically bound dimers (Fig 2c,d) and the lowest energy point on the FES, corresponds to a dimer configuration that closely resemble the crystal structure (Fig 2a).

Surprisingly restriction to a bilayer in MARTINI 2 does not eliminate the presence of non-specifically bound configurations of the LSP1 dimer. While the most stable structure includes the formation of the native dimer interface, the LSP1 deviates slightly from the crystal structure due to a slighlty bent region of the extended tail that forms an additional interface (Fig 2b). In the MARTINI 2 the formation of stable non-native contacts across the protein surface broaden the FES in both 3D and 2D unlike in MARTINI 3 simulations. This has also been observed previously and is a common pitfall of the MARTINI 2 forcefield that stabilizes protein interfaces. Considering the contrasting structural behaviors and energetic differences between the two forcefield versions, one can think of these as effectively different proteins, despite having the same structure, given the substantially different potential energy measurements that result in dramatically more stable binding free energies, as evaluated carefully in a previous work [38]. This is driven by the large de-solvation energy of MARTINI-2, which produces a profoundly stable protein dimer.

Although the statistics on our FES could always be improved via additional sampling, we have compared the surface across multiple time blocks and completeness to assess the confidence of our FES features and shown that the bound ensemble relative to the unbound ensemble are robust (Fig S3, Fig S5).

IV.B The 2D simulations with pseudomembrane restrictions is sufficient to stabilize the crystal state

The FES generated from our 2D simulations that remove the bilayer but retain rigid-body restraints on the monomer's z position and two orientational angles (Methods, Fig S1,2) are remarkably sufficient to stabilize the crystal state of the LSP1 dimer. The free energy of dimerization on the pseudo-membrane is significantly more stable than 3D while not as stable as on an explicit bilayer. Our bilayer is 10% phosphatidylserine and 10% PI(4,5)P_2, with charges of -1 and -4 per molecule, respectively, with the rest composed of the neutral DOPC lipid. This negative charge is important for recruiting the monomers to the surface, where they bind fairly specifically via positively-charged patches of residues. The membrane surface charge also recruits neutralizing counterions in solution changing the local electrostatic environment that possibly contributes to the increased stability observed on the membrane. While the orientational restrictions imposed during the pseudo-membrane simulations do not compensate

for the loss of energetic interactions in presence of a bilayer, they are significant in increasing the sampling specificity of the native bound configurations. This specificity can be attributed to the fairly limited orientational sampling observed for the membrane-bound proteins around their long and short axes (Fig S1,2), which is well-reproduced via our pseudo-membrane simulations in the bound and unbound ensembles (Fig S1,2). In Figure 3, we show the values of the Euler angles that are sampling in both the explicit membrane and pseudo-membrane simulations, illustrating significant reduction in the pitch and roll angles, with unrestricted sampling in the yaw angles.To contrast, our same analysis in 3D shows, as expected, that the individual angles are unrestricted when focusing on a single monomer.

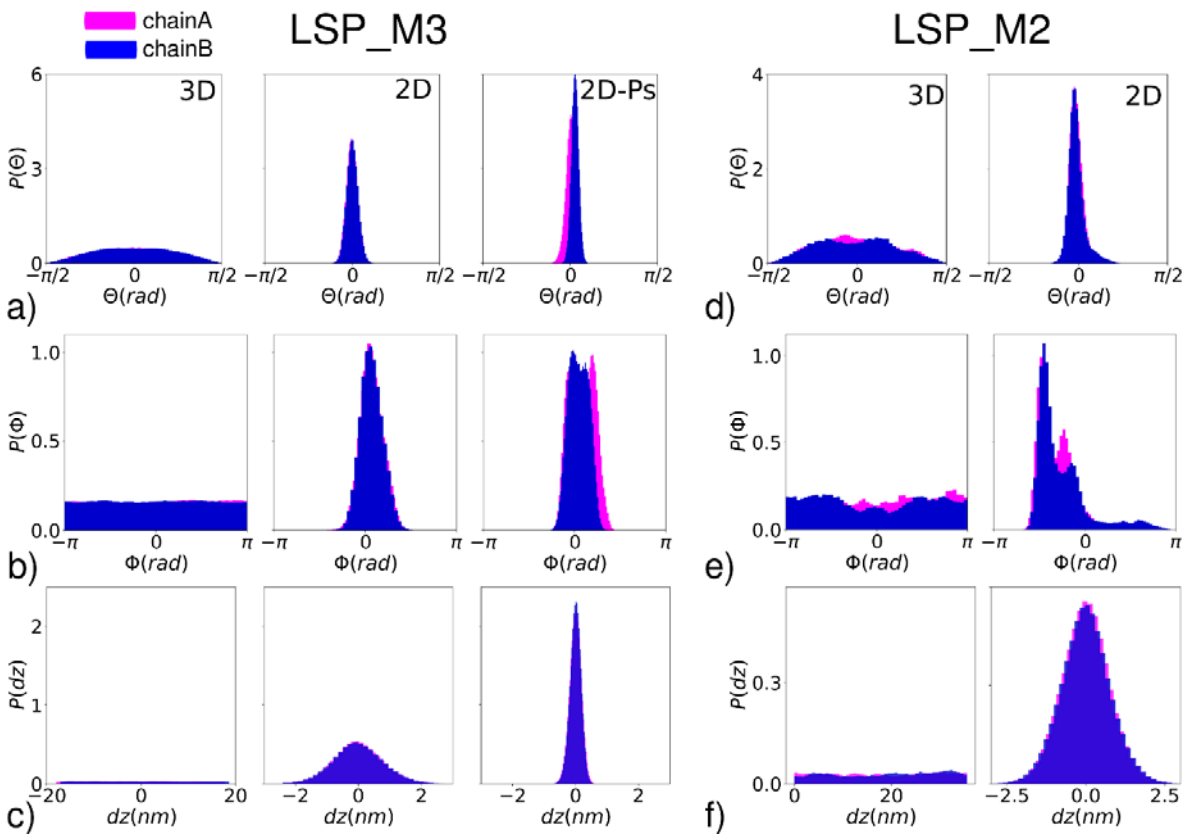

Figure 3 Distribution of the rigid body orientation degrees of freedom for MARTINI 3 and MARTINI 2. a, d) Histogram of the Pitch angle (□) shows uniform distribution in 3D space such that . The distribution on the membrane and pseudo-membrane shows restricted sampling as expected. **b, e)** The roll angle (Φ) also shows uniform sampling when in solution such that , but restricted sampling in the 2D simulations. **c, f)** The yaw angle (□) which evaluates the rotation around the z-axis does not change significantly on the 2D surface and samples all possible values such that .

IV.C The ratio of $\frac{K_D{}^{2D}}{K_D{}^{3D}}$ from simulation is significantly different than a simple rigid-body prediction

From our FES, we can quantify a binding free energy in each environment by partitioning all of the state space into a bound and unbound ensemble. For MARTINI 3 simulations, as shown in Figure 1 and Figure 2c, the FES in 3D is quite distinct from the 2D and pseudo-membrane simulations, which results in a significantly higher estimate of $\Delta G^{3D} = G^{3D}_{bnd} - G^{3D}_{unb}$, compared to $\Delta G^{2D} = G^{2D}_{bnd} - G^{2D}_{unb}$. While we report the instantaneous value of the free energy difference, we performed block averaging to estimate mean values and standard errors associated with each measurement. The free energy differences show a clear shift in lower ΔG^{2D} values for both the explicit membrane and pseudo-membrane simulations (Fig S5, Table 1). As a result, the ratio of $\frac{K_D{}^{2D}}{K_D{}^{3D}}$ is extraordinarily low ($<< 1e^{-3}\ nm$) .

Table 1: Free Energy differences (in kJ/mol) for dimerization in different systems (see Methods).

Integration Mode	MARTINI 3			MARTINI 2	
	3D	2D	2D-Ps	3D	2D
$\Delta G_{t=208\ \mu s}$	-37.89	-91.92	-65.03	-243.75	-261.88
$\langle \Delta G \rangle$	-21.22 ± 7.87	-98.72 ± 6.86	-62.26 ± 5.19	-250.92 ± 28.98	-228.87 ± 11.96

We can use theoretical estimates to predict what $\frac{K_D{}^{2D}}{K_D{}^{3D}}$ would be if our proteins were purely rigid bodies, and if they retained the same (narrow) set of specifically bound structures with the same potential energy difference ΔU between the bound and unbound ensembles in both 3D and 2D. In that case, the change in dissociation constant is purely entropic (see Theory section), Eq. 26, due to reduction in sampling in the z-direction, and the pitch and roll angles. If we measure the loss of configurations from these three variables, we estimate that $\frac{K_D{}^{2D}}{K_D{}^{3D}} \sim 0.03\ nm$ for the explicit membrane, and $\frac{K_D{}^{2D-Ps}}{K_D{}^{3D}} \sim 0.004\ nm$ pseudomembrane (Methods, Table 1). These estimates are significantly larger than the result from our simulations of the full free energy changes, indicating that the assumption that our proteins are rigid bodies and/or the potential energy difference of configurations is unchanged in 3D to 2D is inaccurate

For MARTINI 2 simulations, our estimates of free energy differences reveal that the free energy of dimerization is comparable between the two environments with large standard error associated with the 3D calculation. While this emphasizes the difference between the forcefield versions, the estimates of the lengthscale factor are different between direct estimation from the FES and simple rigid-body approximations. We therefore next assess to what extent the flexibility of our monomers or the potential energy could be driving the huge deviations between our theoretical predictions and our simulations.

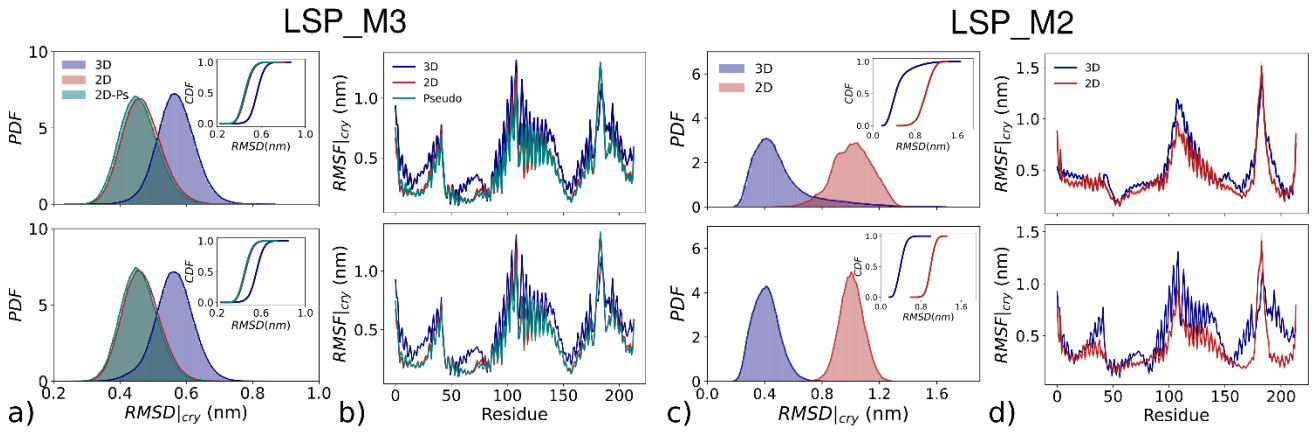

Figure 4 Conformational sampling and flexibility of LSP1 monomer in different environments. a) The RMSD for one protein monomer evaluated w.r.t it's crystal counterpart is evaluated over all bound (top panel) and unbound (lower panel) configurations separately and is shown for the 3 environments in MARTINI 3. The 2D simulations sample monomeric conformational that are closer to the crystal structure configuration. The CDF (inset) also emphasizes the stark contrast in conformations sampled between 2D and 3D. **b**) The RMSF is also evaluated w.r.t to the crystal structure and was calculated for the bound and unbound states by dividing the simulation trajectory into uncorrelated blocks (n_{block} ~ 6-8) and plotting the average (solid line) and the error (shaded region) for each measurement. The monomer chain experiences lower local flexibility in 2D environment. c) RMSD and d) RMSF measurements for MARTINI 2 simulations show different results than MARTINI 3. The LSP1 monomer samples conform closer to it's the crystal counterpart in 3D than in 2D. The RMSF measurements show that it remains more rigid on the 2D membrane than in 3D.

IV.D Configurational sampling while different in 2D does not significantly explain differences in length scale estimates

To go beyond a rigid-body comparison of the sampling in 3D versus 2D, and consider all the internal degrees of freedom, we assessed the fluctuations of our monomeric configurations relative to fixed rigid-body orientations. As guidance, we revisit our theoretical analysis. Our assumptions that produced the purely rigid-body estimate of $\frac{{K_D}^{2D}}{{K_D}^{3D}}$ in Eq. 26 can be relaxed to retain the configurational integrals over all the internal degrees of freedom. We therefore first consider whether this entropy of the internal coordinates is markedly different in 3D vs 2D. To produce the trend observed in our simulations, where $\frac{{K_D}^{2D}}{{K_D}^{3D}}_{SIM} \ll \frac{{K_D}^{2D}}{{K_D}^{3D}}_{RIGID}$, entropically we expect that the unbound ensemble in 3D accesses significantly more states than the unbound ensemble in 2D. These states must be evaluated relative to a fixed rigid-body orientation, as we have already accounted for the loss of rigid-body orientations.

In Figure 4, we compare the RMSD of both monomers to the crystal state, in both the bound and the unbound ensembles and in all 3 environments, as a function of time. Which we can turn into distributions. The distributions show that monomer conformations in 2D are closer to its crystal structure conformation than in 3D. In MARTINI 2 we see the opposite of this behavior as monomers in 3D adopt conformations closer to their crystal structure than in 2D. However, this does not necessarily lead to improved sampling and stability of LSP1 dimeric crystal state in 3D MARTINI 2. The monomers in 2D MARTINI 2 sample conformations away from the crystal state as shown by the RMSD distribution (Fig 4c), however, as seen in the corresponding FES, this does not prevent sampling and stabilization of the LSP1 BAR dimer native interface. We also compute the RMSF of each residue, again averaged separately over the bound and unbound states. The RMSF distributions show similar local flexibilities in large regions of the monomers across different systems, and as expected the regions with membrane binding domains are rigid in 2D systems. Overall, these observations indicate that the discrepancy with the rigid body estimates do not arise from differences in configurational integrals.

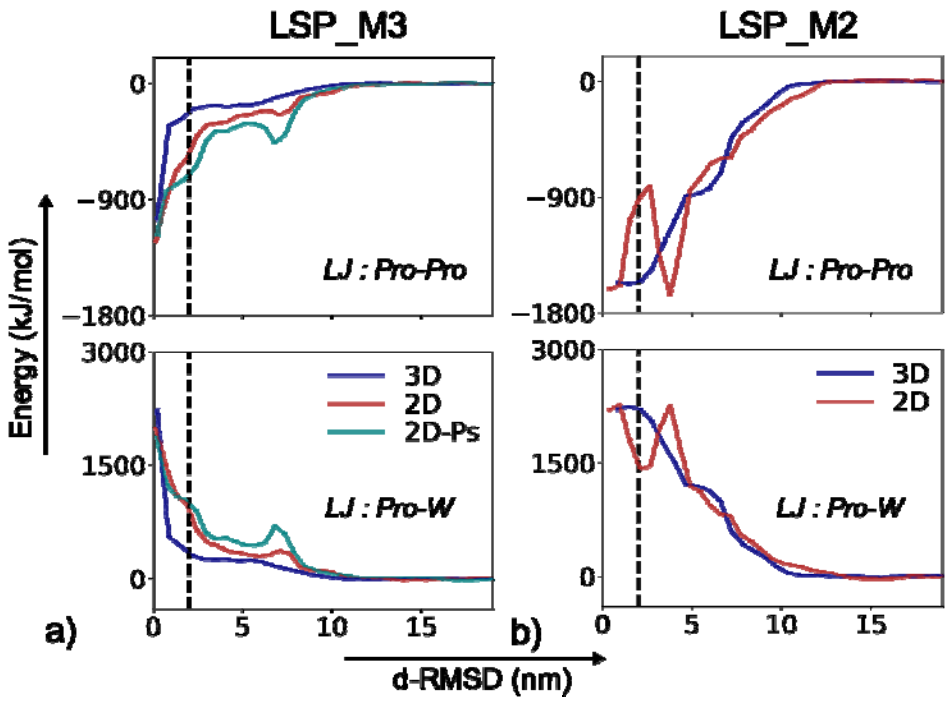

Figure 5 Non-bonded protein interaction energies as a function of dRMSD. The Lennard-jones (LJ) potential values are calculated, for the protein-protein interface (Pro-Pro) and the protein-water interface (Pro-W), for all configurations and mapped to their corresponding dimer-RMSD (dRMSD) values for **a)** MARTINI 3 and **b)** MARTINI 2. For MARTINI 3, the 2D environments have significantly stronger protein-protein interaction energies that stabilize configurations (dRMSD < 2.0 nm ; black dashed line) closer to the crystal structure. In MARTINI 2, both environments experience similar interaction energies.

IV.E The relative potential energies between 3D and 2D strongly bias the 2D crystal state

We can measure the potential energies of all configurations evaluate how it changes between the bound and unbound ensembles by plotting it as a function of dRMSD. We find that the largest energetic contribution towards dimerization arises from the Lennard-Jones interaction energies for the protein-protein interface and the protein-water interface as shown Figure 5. For MARTINI 3, there is a substantial degree of enthalpic stabilization as the protein transitions from the unbound state (dRMSD > 12.0 nm) to the bound state and to the crystal state (dRMSD < 2.0 nm) (Figure 5a). While the minimum energy point of the protein-protein LJ interaction is similar in all 3 environments, it is significantly destabilized as it moves away from the native interface. The protein-water interface acts to destabilize bound state, however the 3D

dimers are not as significantly penalized as the 2D interactions despite having larger solvent accessible surface areas. This indicates that the protein-water has favorable interactions in 3D which act to stabilize non-specifically bound states unlike in the 2D. These observations strongly indicate that discrepancy with the rigid-body estimates arises due to the difference in enthalpic contributions between 3D and 2D.

For MARTINI 2 simulations we observe that the potential energies of interactions are similar in 3D and 2D which support the comparable free energy differences observed in the previous section. We also note that the 2D interaction has a sharp rise in the protein-protein interaction energy around configurations with dRMSD ~ 2nm which could be attributed to poor sampling since we observe only 1 transition to and from the crystal state. We further assessed how the differences (for MARTINI 3) or similarities (for MARTINI 2) between interaction energies affect configurations within the crystal state threshold (dRMSD < 2nm).

IV.F LSP1 dimer samples different binding interfaces in 3D and 2D

The rigid-body assumption that protein dimerization has similar configurational integrals in 3D and 2D arises from the criteria that the two proteins maintain their binding interface during dimerization in the two different environments. Since the presence of native bound state is crucial for BAR dimers, which rely on their intrinsic curvature for membrane remodeling, we looked at how the differences in interaction energies between 3D and 2D impact configurations within the native bound threshold of dRMSD < 2.0 nm. By classifying these configurations into two sets – i) with dRMSD < 0.6 nm (1.0 nm for MARTINI 2) and ii) dRMSD < 2.0 nm we found that the 3D configurations in MARTINI 3 with the larger dRMSD had weaker protein-protein interaction energies than configuration with similar dRMSD in 2D. Importantly while the configurations with lower dRMSD values (< 0.6nm) have similar protein-protein interaction energies between 3D and 2D, they are not as frequently sampled in 3D. This is explained by the protein-water interactions which favor the larger dRMSD configurations energies in 3D (Fig 6a). We also isolated trajectory frames corresponding to these two sets of configurations and represented them in a single snapshot (Fig 6b). The smaller dRMSD configurations show similar structural resemblance between 3D and 2D. However as seen in Figure 2a, these configurations are only stable on the membrane surface. The snapshots of configurations with larger values of dRMSD show a stark contrast between 3D and 2D. These structures

demonstrated how the 3D configurations that are stabilized by protein-water interactions sample widely diverse binding interfaces not observed in 2D.

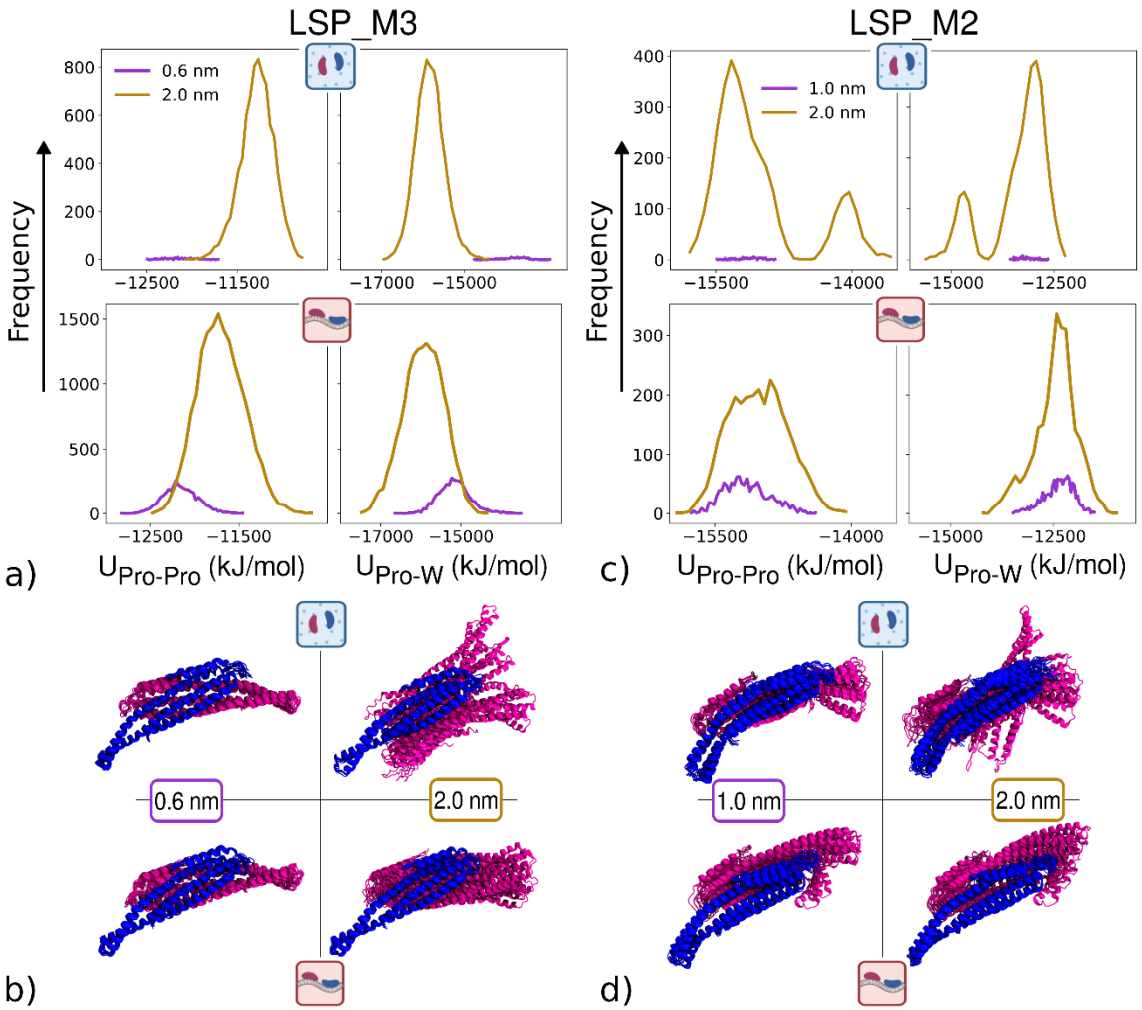

Figure 6 Energetic and configurational sampling of specific dimer states. For LSP1 dimerization we evaluated the interaction energies between the protein-protein and protein-water interface for two mutually exclusive configurational states with dRMSD < 0.6nm and dRMSD <2.0 nm. The configurations represent structures that are closest to the specifically bound BAR dimer state. **a)** The distributions of the interaction energies shows that configurations with 0.6 nm < dRMSD < 2.0 nm (brown) are different in 3D than in 2D, with 3D protein-protein interactions being less stable. The configurations with dRMSD < 0.6 nm (purple) have stable protein-protein interfaces but are sampled in a larger amount in 2D. **b)** Combined trajectory snapshots of LSP1 dimer in the two configurational states. While the configurations

with dRMSD < 0.6 nm are similar, snapshots of with 0.6 nm < dRMSD < 2.0 nm display significantly different conformations. While 2D confirmations maintain their dimeric interface, the configurations in 3D interact through different interfaces that are not as stable. **c)** Distributions of interaction energies for MARTINI 2 simulations. In this case we see that configurations in 3D with 0.6 nm < dRMSD < 2.0 nm sample two states with different energies, with the stable state being closer to the crystal structure and having similar energy as the one with dRMSD< 0.6nm. **d)** Trajectory snapshots show that configurations with dRMSD<0.6nm are slightly different between 3D and 2D in MARTINI 2 but are also very different from their corresponding MARTINI 3 structures. Snapshots of the 3D MARTINI 2 configurations with larger dRMSD values show higher conformational variability corresponding to two distinct energetic states.

In the case of MARTINI 2 simulations, the 3D simulations with larger dRMSD values sample two different sub-states of configurations (Fig 6c). The 3D configurations with the less stable protein-protein interactions are stabilized by protein-water interactions similar to the 3D MARTINI 3 system. However, the protein-water interactions are not as strong since a larger proportion of the configurations are present the sub-state with a more stable protein-protein interaction (left peak (brown) in Fig 6c for 3D). The overlap with the 3D configurations with dRMSD < 1.0 nm and all 2D configurations (dRMSD < 2.0 nm) indicates that this stabilization occurs from forming a more rigid native protein dimer interface. The trajectory snapshots (Fig 6d) show a larger conformational diversity for 3D configurations with higher dRMSD values similar to MARTINI 3. We also observe that the configurations in 2D MARTINI 2 with form a distorted dimeric interface that is different than the ones observed for configurations with dRMSD < 1.0 nm for MARTINI 2 and configurations with dRMSD < 0.6nm for MARTINI 3 which resemble the crystal structure. This also demonstrates how poorly the explicit bilayer biases the native dimer interface in MARTINI 2.

DISCUSSION

We show here how BAR-domain dimerization on the membrane surface has a favorable binding free energy, ΔG^{2D}, that is more selective for the bound state than dimerization in solution, but only for LSP_M3. In contrast, for BAR-domain dimerization of LSP_M2, it is slightly less stable on the membrane. From analysis of our MD simulation data compared to theory, we find that the behavior of LSP_M3 cannot be simply explained by the loss of translational and rotational entropy of the proteins, as would be predicted by the rigid-body approximation for the lengthscale $\frac{{K_D}^{2D}}{{K_D}^{3D}}$ in Eq. 24. Instead, significant changes in the flexibility in the proteins and

stabilizing potential energy of new 2D configurations improves the bound state free energy, reducing the lengthscale $\frac{K_D{}^{2D}}{K_D{}^{3D}}$ to the subnanomolar regime. Somewhat surprisingly, this result was reproduced even when the explicit lipid bilayer was swapped out for a fully-solvated protein subject to rotational and translational 'pseudomembrane' constraints. Thus for the BAR-domain dimerization, the membrane does contribute somewhat, in terms of variations to the electrostatic environment at the surface (e.g. due to the negative charge of the lipid head groups), and perhaps most importantly via enhanced fluctuations in z compared to our pseudo-membrane simulations. Explicit interactions between the proteins and the lipids are also not substantially altering the protein conformations as can happen for less structured proteins[33], and although membrane fluctuations are important for cell-cell adhesion proteins due to the clear distance requirement for interactions[16], the impact here seems to be much less. Instead, our results show the role of the membrane on dimerization is largely geometric: it restricts rigid body motion and this propagates to a loss of flexibility of the protein backbone sampling in both bound and unbound monomers.

Although our result provides a quantitative metric for the 2D binding strength, there are several reasons why we instead emphasize the qualitative features that are conserved across both our MARTINI 2 and MARTINI 3 simulations. Quantitatively, the FES and the $\frac{K_D{}^{2D}}{K_D{}^{3D}}$ lengthscales are both quite different between these two force-fields. However, in both cases, the pseudomembrane simulations agree well with the 2D simulations. Further, by considering the theory behind the $\frac{K_D{}^{2D}}{K_D{}^{3D}}$ presented in Section 2 and by analyzing the entropic and enthalpic contributions to both systems, we are able to explain why the same proteins produce distinct FES when localized to the membrane in different forcefields. The potential energy is lowered for 2D LSP_M3 configurations, but not for the 2D LSP_M2 configurations. Also, while our FES constructed via metadynamics show reasonable convergence, the 2-state free energies are quite sensitive to variations in the surface, and thus produce quite large error bar estimates. The BAR-domain FES is expected to contain more features, in terms of free energy minima, because it contains interfaces to form not only the more stable dimer structure, but higher order oligomer contacts. An alternative to metadynamics that would be particularly informative for this 3D to 2D comparison would be to perform free energy calculations using a cascade of geometric restraints, as they directly operate on Euler angles and translational degrees of freedom[40, 45, 46]. Performing these calculations for all-atom domains would dramatically increase the

computational cost, but we expect it to be more accurate[46] and ideally resolve the discrepancies between the two CG force-fields used here.

Despite not having access to experimental measurements of the ${K_D}^{2D}$ for peripheral membrane proteins like the BAR-domain containing proteins, experimental data from in vitro studies support that the $\frac{{K_D}^{2D}}{{K_D}^{3D}}$ lengthscale will be below the micrometer regime of a typical $\frac{V_1}{SA_1}$ system. While measurements of BAR-domain dimerization are convoluted by the fact that the dimers can then form higher-order oligomers[14], which introduces a distinct protein-protein interface and corresponding $\frac{{K_D}^{2D}}{{K_D}^{3D}}$ lengthscale, experiments find significant increases in oligomerization (and thus dimerization) on membranes compared to in solution for a variety of BAR proteins [14, 47-49]. At least one of these lengthscales therefore favors 2D assembly via dimensional reduction. This is also supported by the known thermodynamics of BAR domains in solution; the BAR-domain proteins human endophilin 1 and FCHo2 have measured dimerization ${K_D}^{3D}$'s of ~1μM[9, 10, 50], but both proteins have concentrations more than 10x less than this in HeLa cells[51]. The oligomerization strength for BAR dimers is clearly weaker than dimerization as they are not observed to form oligomers at dimer-forming concentrations[10, 50], and collectively, these numbers indicate that these proteins would form minimal dimers in the cytoplasm on their own. In vivo, BAR-domain proteins clearly form assemblies on membranes[14, 20]. While in vivo observations are of course always complicated by the many other protein interactions that can compete or cooperate to form assemblies, many BAR-domain partners are also peripheral membrane proteins[52], meaning they could contribute to assembly stability in either 3D or 2D, but seem to clearly bias towards 2D. The LSP1 protein we study here, for instance, can form dimers and even oligomers in solution in vitro[18, 53], but in vivo it forms large oligomeric scaffolds called eisosomes containing thousands of LSP1 proteins on the plasma membrane[19], with only small cytoplasmic complexes observed[20]. We note that BAR-domain proteins form membrane-bound oligomers that can cause dramatic tubulation and sculpting of membranes in vitro[48, 54, 55], even driving membrane fission[56]. The ability of BAR-domain proteins to both sense curvature (bind preferentially to high curvature) and induce curvature means that the affinities for the membrane are curvature dependent [57, 58], but so might be the affinities for one another (${K_D}^{2D}$). While we do not anticipate a dramatic curvature dependence for the protein dimer ${K_D}^{2D}$ given its small size, the curved structure of the oligomer likely favors more stable filaments (stronger ${K_D}^{2D}$) on highly curved membranes. We emphasize that regardless of any mechanical or curvature dependencies that could

impact ${K_D}^{2D}$, the fundamental thermodynamic relationships favoring binding in 3D or 2D ($\frac{{K_D}^{2D}}{{K_D}^{3D}} < \frac{V_1}{SA_1}$) remains unchanged. However, the size of the resulting equilibrium population of dimers and oligomers will depend on the mechanical and chemical properties of the membrane[58] that control ${K_D}^{2D}$ and the localization affinity[22].

Overall, a key finding of this study is that the binding between peripheral membrane proteins on the 2D membrane is favorable relative to 3D. Assembly within 2D must be considered an important mechanism for assembly even in nonequilibrium environments. Diffusion in 2D is at least 100x slower than 3D, but for physiologic concentrations, it can still greatly facilitate binding, more so than 3D recruitment as found for dynamin oligomerization at endocytic sites[59]. Our results do not report on the kinetics of binding in 2D, but the on-rates will have a similar lengthscale controlling the 3D vs the 2D association. If the off-rates are the same in 3D and 2D, this will be the same as the thermodynamic value, but generally speaking, it can take on a potentially wider range of values. Rate 'constants' in 2D are also not truly constant due to reentrant diffusion, unlike in 3D[60], which complicates their estimation. Understanding the determinants of these fundamental 2D vs 3D binding metrics is critical to constructing accurate models for cell systems.

REFERENCES

1. Ehrlich, M., et al., *Endocytosis by random initiation and stabilization of clathrin-coated pits.* Cell, 2004. **118**(5): p. 591-605.
2. Kaksonen, M. and A. Roux, *Mechanisms of clathrin-mediated endocytosis.* Nat Rev Mol Cell Biol, 2018. **19**(5): p. 313-326.
3. Sigismund, S., et al., *Endocytosis in the context-dependent regulation of individual and collective cell properties.* Nat Rev Mol Cell Biol, 2021. **22**(9): p. 625-643.
4. Haugh, J.M. and D.A. Lauffenburger, *Physical modulation of intracellular signaling processes by locational regulation.* Biophys J, 1997. **72**(5): p. 2014-31.

5. Sorkin, A. and M. von Zastrow, *Endocytosis and signalling: intertwining molecular networks.* Nat Rev Mol Cell Biol, 2009. **10**(9): p. 609-22.
6. Alfonzo-Mendez, M.A., et al., *Dual clathrin and integrin signaling systems regulate growth factor receptor activation.* Nat Commun, 2022. **13**(1): p. 905.
7. Denk, J., et al., *MinE conformational switching confers robustness on self-organized Min protein patterns.* Proc Natl Acad Sci U S A, 2018. **115**(18): p. 4553-4558.
8. Brauns, F., et al., *Bulk-surface coupling identifies the mechanistic connection between Min-protein patterns in vivo and in vitro.* Nat Commun, 2021. **12**(1): p. 3312.
9. Capraro, B.R., et al., *Kinetics of endophilin N-BAR domain dimerization and membrane interactions.* J Biol Chem, 2013. **288**(18): p. 12533-43.
10. Gallop, J.L., et al., *Mechanism of endophilin N-BAR domain-mediated membrane curvature.* EMBO J, 2006. **25**(12): p. 2898-910.
11. Wakeham, D.E., et al., *Clathrin self-assembly involves coordinated weak interactions favorable for cellular regulation.* EMBO J, 2003. **22**(19): p. 4980-90.
12. Rosendale, M., et al., *Functional recruitment of dynamin requires multimeric interactions for efficient endocytosis.* Nat Commun, 2019. **10**(1): p. 4462.
13. Gallego, O., et al., *A systematic screen for protein-lipid interactions in Saccharomyces cerevisiae.* Molecular Systems Biology, 2010. **6**.
14. Peter, B.J., et al., *BAR domains as sensors of membrane curvature: the amphiphysin BAR structure.* Science, 2004. **303**(5657): p. 495-9.
15. Hu, J., R. Lipowsky, and T.R. Weikl, *Binding constants of membrane-anchored receptors and ligands depend strongly on the nanoscale roughness of membranes.* Proc Natl Acad Sci U S A, 2013. **110**(38): p. 15283-8.
16. Xu, G.K., et al., *Binding constants of membrane-anchored receptors and ligands: A general theory corroborated by Monte Carlo simulations.* J Chem Phys, 2015. **143**(24): p. 243136.
17. Laio, A. and F.L. Gervasio, *Metadynamics: a method to simulate rare eventsand reconstruct the free energy in biophysics,chemistry and material science.* Rep. Prog. Phys., 2008. **71**: p. 126601.
18. Ziolkowska, N.E., et al., *Eisosome-driven plasma membrane organization is mediated by BAR domains.* Nat Struct Mol Biol, 2011. **18**(7): p. 854-6.
19. Olivera-Couto, A., et al., *The eisosome core is composed of BAR domain proteins.* Mol Biol Cell, 2011. **22**(13): p. 2360-72.

20. Olivera-Couto, A., et al., *Eisosomes are dynamic plasma membrane domains showing pil1-lsp1 heteroligomer binding equilibrium.* Biophys J, 2015. **108**(7): p. 1633-1644.
21. Le Chatelier, H.L., Ann. des Mines, 1888. **13**: p. 157.
22. Yogurtcu, O.N. and M.E. Johnson, *Cytosolic proteins can exploit membrane localization to trigger functional assembly.* PLoS Comput Biol, 2018. **14**(3): p. e1006031.
23. Adam, G. and M. Delbruck, *Reduction of Dimensionality in Biological Diffusion Processes*, in *Structural Chemistry and Molecular Biology*. 1968, Freeman: San Francisco. p. 198-215.
24. Berg, H.C. and E.M. Purcell, *Physics of Chemoreception.* Biophysical Journal, 1977. **20**(2): p. 193-219.
25. Wu, Y., et al., *Transforming binding affinities from three dimensions to two with application to cadherin clustering.* Nature, 2011. **475**(7357): p. 510-3.
26. Adrien, V., et al., *Kinetic study of membrane protein interactions: from three to two dimensions.* Sci Rep, 2024. **14**(1): p. 882.
27. Gavutis, M., et al., *Lateral ligand-receptor interactions on membranes probed by simultaneous fluorescence-interference detection.* Biophys J, 2005. **88**(6): p. 4289-302.
28. Gavutis, M., S. Lata, and J. Piehler, *Probing 2-dimensional protein-protein interactions on model membranes.* Nat Protoc, 2006. **1**(4): p. 2091-103.
29. Gavutis, M., et al., *Determination of the two-dimensional interaction rate constants of a cytokine receptor complex.* Biophys J, 2006. **90**(9): p. 3345-55.
30. Pucadyil, T.J. and S.S. Holkar, *Comparative analysis of adaptor-mediated clathrin assembly reveals general principles for adaptor clustering.* Mol Biol Cell, 2016. **27**(20): p. 3156-3163.
31. Guo, S.-K., A.J. Sodt, and M.E. Johnson, *Large self-assembled clathrin lattices spontaneously disassemble without sufficient adaptor proteins.* PLOS Computational Biology, 2022. **18**(3): p. e1009969.
32. Kirchhausen, T. and S.C. Harrison, *Protein organization in clathrin trimers.* Cell, 1981. **23**(3): p. 755-61.
33. Krausser, J., T.P.J. Knowles, and A. Saric, *Physical mechanisms of amyloid nucleation on fluid membranes.* Proc Natl Acad Sci U S A, 2020. **117**(52): p. 33090-33098.
34. Souza, P.C.T., et al., *Protein-ligand binding with the coarse-grained Martini model.* Nat Commun, 2020. **11**(1): p. 3714.
35. Alessandri, R., et al., *Pitfalls of the Martini Model.* J Chem Theory Comput, 2019. **15**(10): p. 5448-5460.

36. Bonomi, M., et al., *PLUMED: A portable plugin for free-energy calculations with molecular dynamics.* Computer Physics Communications, 2009. **180**(10): p. 1961-1972.

37. Berendsen, H.J.C., D. Vanderspoel, and R. Vandrunen, *Gromacs - a Message-Passing Parallel Molecular-Dynamics Implementation.* Computer Physics Communications, 1995. **91**(1-3): p. 43-56.

38. Jhaveri, A., et al., *Thermodynamics and free energy landscape of BAR-domain dimerization from molecular simulations.* J Phys Chem B, 2021. **125**: p. 3739-3751.

39. Gilson, M.K., et al., *The statistical-thermodynamic basis for computation of binding affinities: a critical review.* Biophys J, 1997. **72**(3): p. 1047-69.

40. Woo, H.J. and B. Roux, *Calculation of absolute protein-ligand binding free energy from computer simulations.* Proc Natl Acad Sci U S A, 2005. **102**(19): p. 6825-30.

41. Weikl, T.R., et al., *Binding equilibrium and kinetics of membrane-anchored receptors and ligands in cell adhesion: Insights from computational model systems and theory.* Cell Adh Migr, 2016. **10**(5): p. 576-589.

42. Souza, P.C.T., et al., *Martini 3: a general purpose force field for coarse-grained molecular dynamics.* Nat Methods, 2021. **18**(4): p. 382-388.

43. de Jong, D.H., et al., *Improved Parameters for the Martini Coarse-Grained Protein Force Field.* J Chem Theory Comput, 2013. **9**(1): p. 687-97.

44. Tiwary, P. and M. Parrinello, *A time-independent free energy estimator for metadynamics.* J Phys Chem B, 2015. **119**(3): p. 736-42.

45. Fu, H., et al., *Accurate determination of protein:ligand standard binding free energies from molecular dynamics simulations.* Nat Protoc, 2022. **17**(4): p. 1114-1141.

46. Blazhynska, M., et al., *Hazardous Shortcuts in Standard Binding Free Energy Calculations.* J Phys Chem Lett, 2022. **13**(27): p. 6250-6258.

47. Mondal, S., et al., *Endophilin recruitment drives membrane curvature generation through coincidence detection of GPCR loop interactions and negative lipid charge.* J Biol Chem, 2021. **296**: p. 100140.

48. Gallop, J.L. and H.T. McMahon, *BAR domains and membrane curvature: bringing your curves to the BAR.* Biochem Soc Symp, 2005(72): p. 223-31.

49. Zeno, W.F., et al., *Synergy between intrinsically disordered domains and structured proteins amplifies membrane curvature sensing.* Nat Commun, 2018. **9**(1): p. 4152.

50. Henne, W.M., et al., *Structure and analysis of FCHo2 F-BAR domain: a dimerizing and membrane recruitment module that effects membrane curvature.* Structure, 2007. **15**(7): p. 839-52.

51. Hein, M.Y., et al., *A human interactome in three quantitative dimensions organized by stoichiometries and abundances.* Cell, 2015. **163**(3): p. 712-23.

52. Duan, D., et al., *Integrating protein copy numbers with interaction networks to quantify stoichiometry in clathrin-mediated endocytosis.* Sci Rep, 2022. **12**(1): p. 5413.

53. Karotki, L., et al., *Eisosome proteins assemble into a membrane scaffold.* J Cell Biol, 2011. **195**(5): p. 889-902.

54. Ayton, G.S., et al., *New Insights into BAR Domain-Induced Membrane Remodeling.* Biophysical Journal, 2009. **97**(6): p. 1616-1625.

55. Ayton, G.S. and G.A. Voth, *Multiscale simulation of protein mediated membrane remodeling.* Semin Cell Dev Biol, 2010. **21**(4): p. 357-62.

56. Snead, W.T., et al., *BAR scaffolds drive membrane fission by crowding disordered domains.* J Cell Biol, 2019. **218**(2): p. 664-682.

57. Zhu, C., S.L. Das, and T. Baumgart, *Nonlinear sorting, curvature generation, and crowding of endophilin N-BAR on tubular membranes.* Biophys J, 2012. **102**(8): p. 1837-45.

58. Shi, Z. and T. Baumgart, *Membrane tension and peripheral protein density mediate membrane shape transitions.* Nat Commun, 2015. **6**: p. 5974.

59. Jiang, A., et al., *Dynamin1 long- and short-tail isoforms exploit distinct recruitment and spatial patterns to form endocytic nanoclusters.* Nat Commun, 2024. **15**(1): p. 4060.

60. Yogurtcu, O.N. and M.E. Johnson, *Theory of bi-molecular association dynamics in 2D for accurate model and experimental parameterization of binding rates.* Journal of Chemical Physics, 2015. **143**(8): p. 084117.